Professional Leave Report Cover Sheet

Name: Deify Law

Department: Mechanical Engineering

College: Lyles College of Engineering

Leave taken: ◉ Sabbatical ○ Difference in Pay ○ Professional Leave without Pay

Time Period: ◉ Fall 2021

○ Spring

○ Academic Year

○ Other

Your report will be sent to your Dean for your PAF and to the Library Archives.

**Fall 2021 Sabbatical Report** March 30, 2022

Name: Deify Law
Department: Mechanical Engineering
Rank: Associate Professor

## Introduction

My Sabbatical was taken during the Fall 2021 semester. I spent my Sabbatical conducting fluid mechanics research and observing thermo-fluid lecture and laboratory class teachings at the University of St. Thomas in the city of St. Paul, Minnesota. I met my collaborator Dr. Thomas Shepard on the first day of my arrival to go over the plans of the proposed fluid mechanics research works and the proposed lecture and laboratory teaching observations. My Sabbatical objectives are twofold: research and teaching objectives. For research objectives, I proposed to be involved in both experimental and numerical works of studying the dynamics of single and multiple air bubbles in a converging nozzle as well as investigating the impact of aspect ratio on drag and flow structure for cylinders with two free ends in a wind-tunnel setting experimentally and numerically. I have accomplished both proposed research objectives during my Sabbatical. In addition, I have also accomplished several new research tasks during my Sabbatical, and they include bubbly flow and heat transfer enhancement modeling, nanofluid and heat transfer modeling, and experimental study of indoor air quality. The products include two peer-reviewed conference publications and one technical report publication. For teaching objectives, I proposed to participate in conducting wind-tunnel experiments using National Instruments data acquisition and LabVIEW setup and instrumentation as well as observing thermo-fluid lecture and laboratory classes in person. I have accomplished both proposed teaching objectives during my Sabbatical. All accomplished research and teaching objectives are listed as follows:

**1. Accomplished Research Objectives**:

1. Dynamics of single and multiple air bubbles in a converging nozzle (**accomplished proposed task**)
2. Impact of aspect ratio on drag and flow structure for cylinders with two free ends (**accomplished proposed task, work is accepted for a peer-reviewed conference publication**)
3. Effect of bubble sizes and void fractions on thermal transport in homogeneous bubbly flow: Eulerian-Eulerian modeling (**accomplished new task**)
4. Effect of a single nanoparticle diameter size on a nanochannel fluid flow and heat transfer (**accomplished new task, work is accepted for a peer-reviewed conference publication**)
5. A mitigation study of air treatment technology with a physical air filter on volatile organic compounds, carbon dioxide, and fine particulate matters generated by indoor smoke (**accomplished new task, final report is submitted to ASHRAE San Joaquin Chapter**)

**2. Accomplished Teaching Objectives**:

1. Wind-tunnel National Instruments data acquisition and LabVIEW setup and instrumentation (**accomplished proposed task**)

2. Thermo-fluid classroom and laboratory teaching observations (**accomplished proposed task**)

Specific **1. research** and **2. teaching** tasks conducted during my Sabbatical are detailed as follows:

**Research**

**1.1.** Dynamics of single and multiple air bubbles in a converging nozzle

I spent a major part of my Sabbatical time performing both experimental and numerical works of this proposed research. The experimental test channel shown in Fig.1 was constructed of three layers to allow the bubbles to be backlit and captured with a high-speed camera shown in Fig.2. The two outside layers were clear acrylic windows while in inside layer, which defined to internal flow geometry, was machined from aluminum. The total internal channel dimensions were 162 mm long x 12 mm wide x 8 mm high. Water entered from the top of the channel and flowed vertically downward. Air was injected though a 2.9 mm hole positioned 68 mm upstream of the exit. The channel converges at 45 degrees to a 2 mm diameter exit orifice that is 3 mm long and the flow exited to ambient conditions. Tap water was pumped via a rotary vane pump and measured using a calibrated turbine flow meter (SeaMetric SPX-075). Compressed air flow was controlled by a pressure regulator and measured using a mass flow meter (Alicat Scientific).

A Photron SA1.1 high-speed camera fitted with a 12X zoom lens (Navitar) was used to capture images of the bubble dynamics near the channel exit at 5400 frames per second. The flow was backlit using an LED light source (Bridgelux BXRC-50C10K0-04). An algorithm developed in MATLAB tracked the top-most and bottom-most position of a bubble as it approached the convergent section and deformed to the exit orifice. The experimental bubble diameters were determined as the equivalent diameter for the projected area of the bubble prior to entering the convergent nozzle section of the channel. The equivalent diameter was used since the bubbles were not perfectly spherical, and an oscillation was noted in their shapes as they moved downward through the channel.

The overall test facility is shown in Fig. 3. By adjusting the air flow rate bubbles of varying size could be generated. For the conditions studied in this work, the liquid flow rate was set to 1.82 LPM. In creating the smaller of the bubbles considered (D = 4.29 mm) the air flow rate was 0.58 SLPM. In creating the larger of the bubbles considered (D = 8.7 mm) the air flow rate was 1.00 SLPM.

**Figure 1.** Test apparatus of a converging nozzle

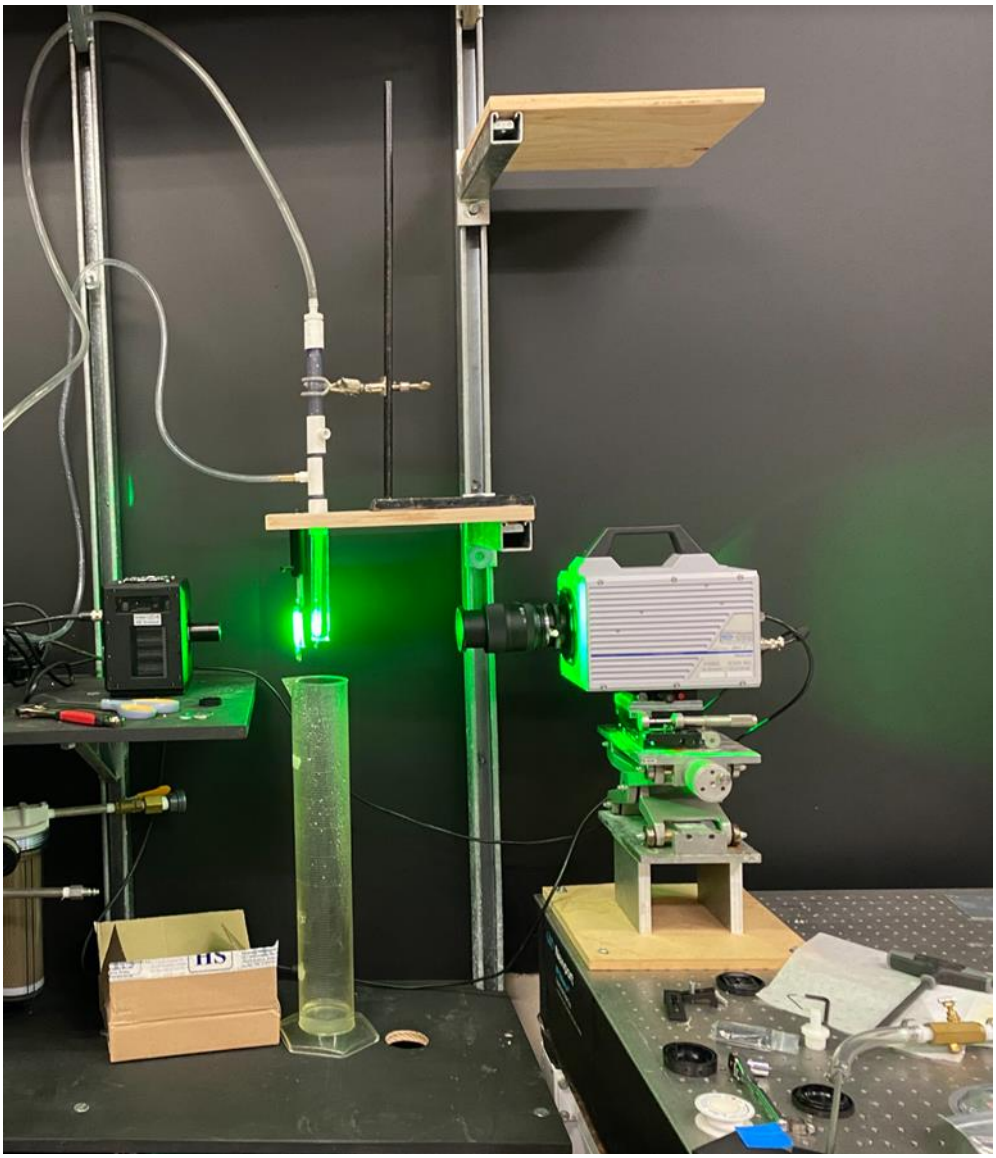

**Figure 2.** Converging nozzle is backlit and captured with a high-speed camera

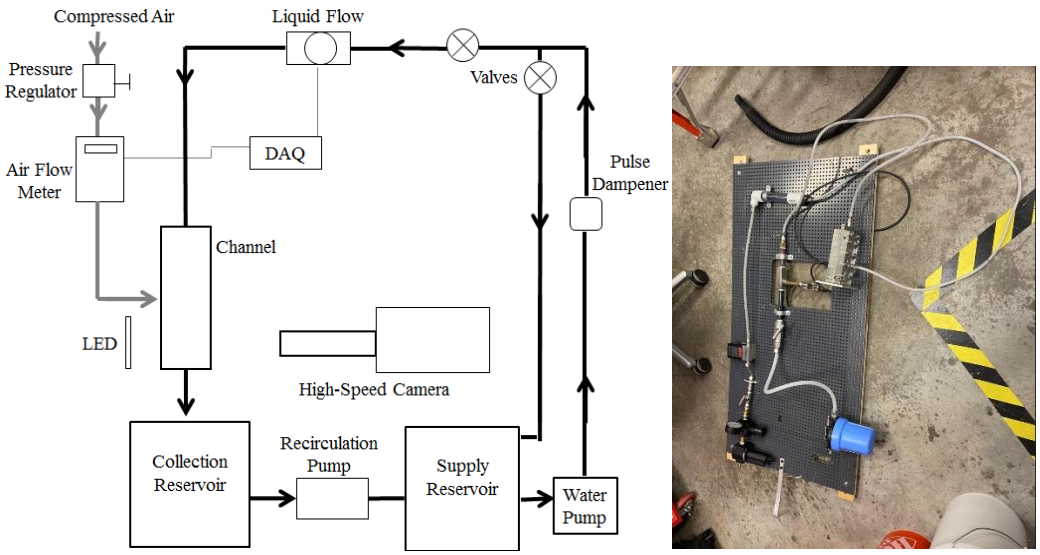


**FIGURE 3.** Schematic and Experimental Setup

The volume of fluid (VOF) model is employed to model two immiscible fluids by solving a single set of momentum equations and tracking the volume fraction of each of the fluids throughout the domain. The subscript c refers to the continuous phase and the subscript d refers to the dispersed phase. The continuity equations for each phase, neglecting mass transfer, are:

$$\frac{\partial}{\partial t}(\alpha_c \rho_c) + \nabla \cdot (\alpha_c \rho_c \vec{u}_c) = 0 \tag{1}$$

$$\frac{\partial}{\partial t}(\alpha_d \rho_d) + \nabla \cdot (\alpha_d \rho_d \vec{u}_d) = 0 \tag{2}$$

In each control volume, the volume fractions of all phases sum to unity. The fields for all variables and properties are shared by the phases and represent the volume-averaged values with the volume fraction of each of the phases known at each location.

The properties appearing in the transport equations are determined by the presence of the component phases in each control volume. The volume-fraction-averaged density and dynamic viscosity are:

$$\rho = \alpha_d \rho_d + \alpha_c \rho_c \tag{3}$$

$$\mu = \alpha_d \mu_d + \alpha_c \mu_c \tag{4}$$

A single momentum equation is solved throughout the domain, and the resulting velocity field is shared among the phases. The momentum equation is:

$$\frac{\partial}{\partial t}(\rho \vec{u}) + \nabla \cdot (\rho \vec{u} \vec{u}) = -\nabla p + \nabla \cdot \left[ \mu \left( \nabla \vec{u} + \nabla \vec{u}^T \right) \right] + \vec{F} + \rho \vec{g} \tag{5}$$

where $\vec{F}$ is the surface tension vector. Our surface tension model is based on a continuum surface force (CSF) model. With this model, the addition of surface tension to the VOF calculation results in a source term in the momentum equation. The surface tension is:

$$\vec{F} = \sigma_{cd} \frac{\rho \kappa_c \vec{\nabla} \alpha_c}{\frac{1}{2}(\rho_c + \rho_d)} \tag{6}$$

$$\kappa_c = \vec{\nabla} \cdot \hat{n} \tag{7}$$

$$\hat{n} = \frac{\vec{n}}{|\vec{n}|} \tag{8}$$

$$\vec{n} = \vec{\nabla} \alpha_c \tag{9}$$

where $\sigma_{cd}$ is the surface tension coefficient at 0.0728 N/m between continuous (water) and dispersed (air) phases; $\vec{n}$ is the surface normal vector; $\kappa_c$ is the curvature and it is defined in terms of the divergence of the unit normal $\vec{n}$.

CFD code ANSYS FLUENT is used for the VOF simulations presented in the present work. It must be noted that the present work intends to employ three-dimensional (3D) simulations to improve results of previously conducted two-dimensional (2D) simulations in the previous work of Law et al. 3D simulations are conducted to match the experimental conditions for a modeled flat rectangular channel shown in Fig. 1. The modeled height of the atomizer including a 3 mm long and 2 mm diameter exit orifice is 77.8 mm whereas channel depth and width are 8 mm and 12 mm, respectively. This geometry is identical to the lower part of the experimental set-up and includes a 45$^o$ convergent section. An air bubble with a specified diameter size is initialized near the top of the atomizer whereas water flows downward uniformly at 0.32 m/s through the top section of the atomizer. A no-slip boundary condition is applied for both phases at the walls of the atomizer and an ambient pressure condition is specified at the nozzle exit. The present work employs a grid resolution of 500290 tetrahedral grid cells and a fixed time step of 0.00001 s, which are 173 times more and 10 times less than the 2D settings, respectively, for all simulations to march the solution forward until the entire bubble exits the nozzle. A convergence criterion is set to $1 \times 10^{-7}$ for all dependent variables. Second order upwind discretization is used to discretize the convective terms of all the equations, except the volume fraction equation, for which the QUICK scheme is employed.

The experimental apparatus allowed for gross control of bubble size and bubble shape was not perfectly spherical. One consequence of this is that the simulation and experimental bubble comparisons are of bubbles with similar diameters, but not identical diameters. For this reason, the results presented are expected to compare well qualitatively though exact quantitative comparisons may be a slightly off.

Figures 4-5 compare the deformation of bubbles experiencing deformation during acceleration for the experiment and simulation. While the qualitative results of the previously used two-dimensional simulation compared well under similar conditions, it is

noted that the current three-dimensional simulation shows even better agreement. This is particularly true in capturing the initial necking down of the leading bubble edge during the strong acceleration caused by the contraction ratio of nearly 31. One of the limitations of the two-dimensional simulation arose from matching channel axis geometry as opposed to contraction ratio at the exit.

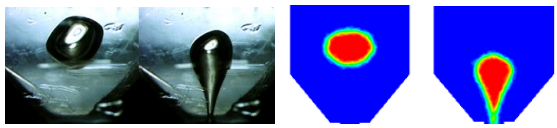

**FIGURE 4.** Comparison of experiment (D = 4.29 mm) and simulation (D = 3 mm) for bubble before and during acceleration

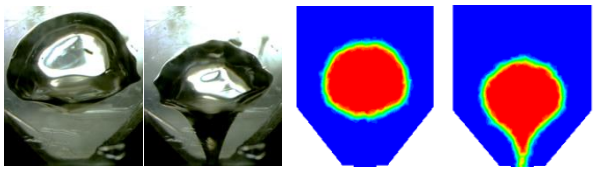

**FIGURE 5.** Comparison of experiment (D = 8.7 mm) and simulation (D = 7 mm) for bubble before and during acceleration

Figures 6-7 present experimental and simulation time traces of the leading and trailing edges of an individual bubble approaching the convergent channel section and exhausting through the nozzle exit for different bubble sizes. The solid horizontal black line in these figures shows the position where channel convergence begins. The bubble acceleration can be noted in these plots by the slope of the trajectory becoming steeper – for example, when the leading edge of the bubble gets to the convergent section.

As noted previously, the trailing edge of the bubble is shown to start accelerating when the leading edge of the bubble reaches the nozzle exit, even if the trailing edge has not reached the convergent section of the channel. This behavior is captured both by the experimental data and the simulation results. One of the biggest discrepancies previously found with the two-dimensional model was its inability to capture this interesting effect. Thus, the current study provides increased evidence for the utility of the three-dimensional numerical technique as a valid tool for understanding the complicated nature of highly accelerating and deforming bubble dynamics.

There are a couple of discrepancies between the experimental and predicted time trace of bubble position. These include different bubble velocity as well as different bubble diameter in the constant area section of the atomizer. These discrepancies will be addressed with a consistent setting in future work.

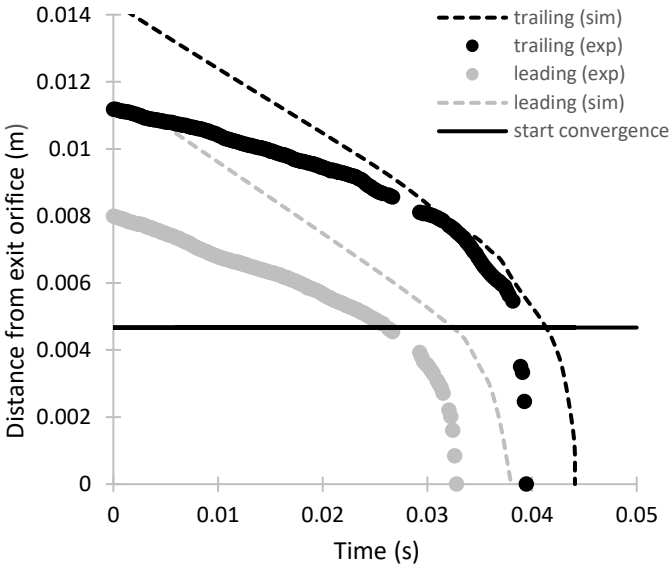


**FIGURE 6.** Leading and trailing bubble edge trajectory comparison between experiment (D = 4.29 mm) and simulation (D = 3 mm)

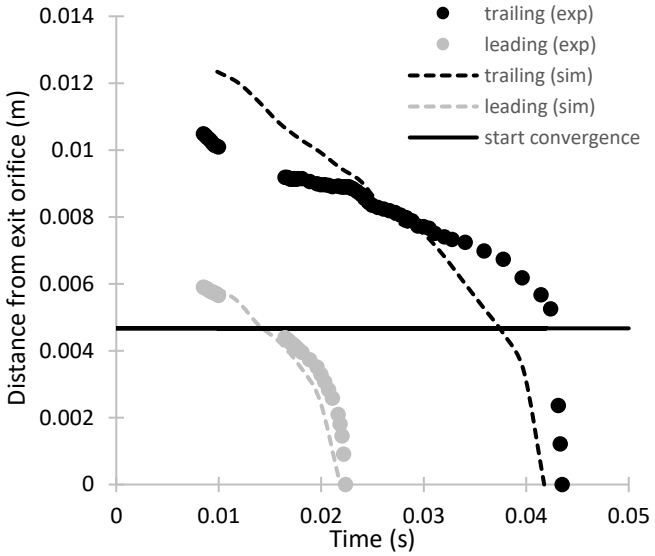


**FIGURE 7.** Leading and trailing bubble edge trajectory comparison between experiment (D = 8.7 mm) and simulation (D = 7 mm)

With increased confidence in the validity of the three-dimensional simulation, its results can be further utilized to understand physical phenomenon that would be more difficult to capture experimentally. Figure 8 presents the average exit velocity of the nozzle as a bubble approaches and exhausts out. For both bubble size conditions, a fluctuation in the exit velocity is seen. For the D = 3 mm bubble the velocity quickly increases from 12.8 to 17 m/s and then drops back to ~ 12.8 m/s. Similarly, for the D = 7 mm bubble diameter the exit velocity jumps from 12.5 to 16.2 m/s exit and then drops back to ~12.5 m/s. These represents a ~30% fluctuation in the mixture exit velocity

caused by the passing of a bubble. These fluctuations are much more significant than those predicted by the previously used two-dimensional model of ~5% [1].

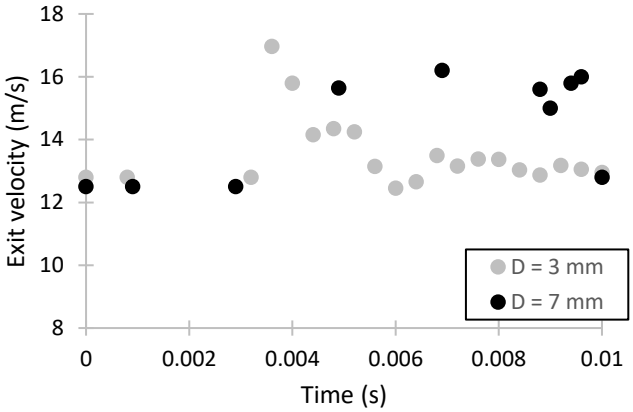


**FIGURE 8.** Simulated exit mixture velocity as bubbles approach and exit

There is an additional consequence to the fluctuation in exit velocity caused by a bubble exiting the channel. If the flow at the exit speeds up, then correspondingly the flow upstream in the channel will also speed up. This is seen by the trailing edge of the bubbles accelerating before reaching the convergent section of the nozzle (Figs. 6, 7). However, the opposite should occur then when the trailing edge of the bubble reaches the exit. Namely, since the exit velocity decreases so should the velocity upstream in the channel after the bubble exits. This behavior was seen in experimental conditions captured by the high-speed camera. Figure 9 shows a slug of air just before it finishes leaving the channel with a bubble trailing behind. After the slug of air has exhausted through the exit, the trailing bubble experiences a notable deceleration. The time trace of the trailing bubble in Fig. 10 clearly shows a decrease in slope after the slug exits providing evidence of the deceleration. Figure 11 reports experimental time trace of two small bubble (approximately 4 mm diameter size) leading and trailing edges. The bubble 1 accelerates rapidly towards the nozzle exit as it approaches the convergent section of the nozzle, and it does not seem to affect the acceleration of the bubble 2. Figure 12 shows the experimental time trace of one big and small bubble (approximately 6 mm and 3 mm diameter sizes, respectively) leading and trailing edges. Similarly, the big bubble accelerates towards the nozzle exit as soon as it reaches the convergent section of the nozzle, and it does not affect the motion of the small bubble significantly. This research is currently a work in progress.

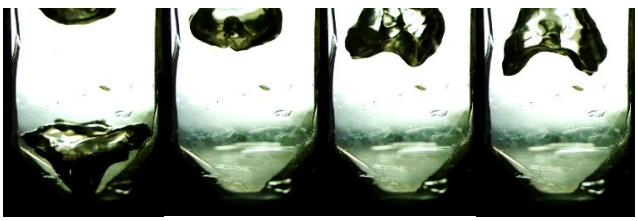

**FIGURE 9.** Deceleration following exit of air slug (5.56 ms between images)

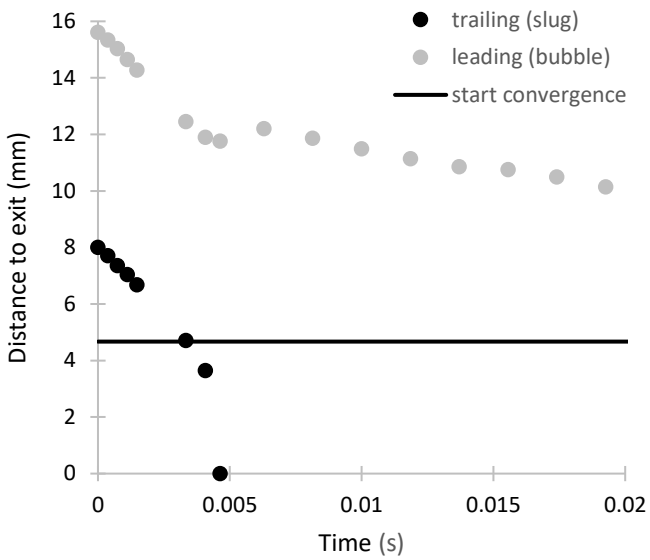


**FIGURE 10.** Experimental time trace of air slug trailing edge and following bubble leading edge in Fig. 7

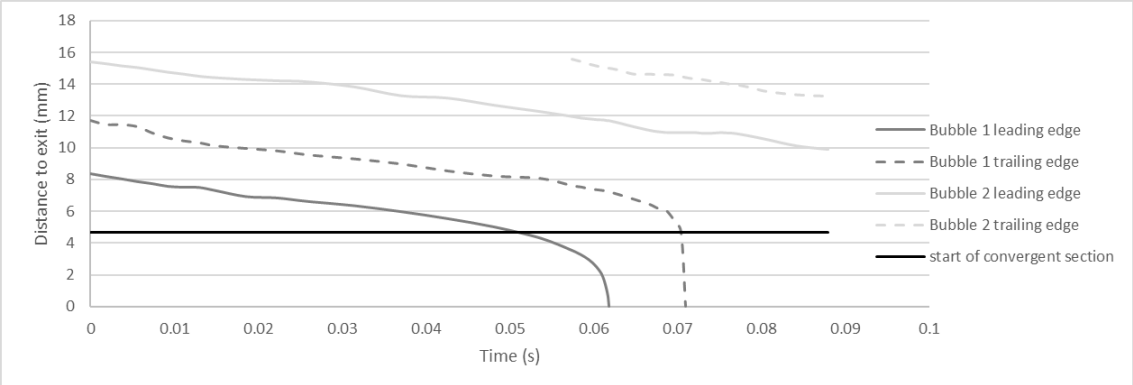


**FIGURE 11.** Experimental time trace of two small bubble (approximately 4 mm diameter size) leading and trailing edges

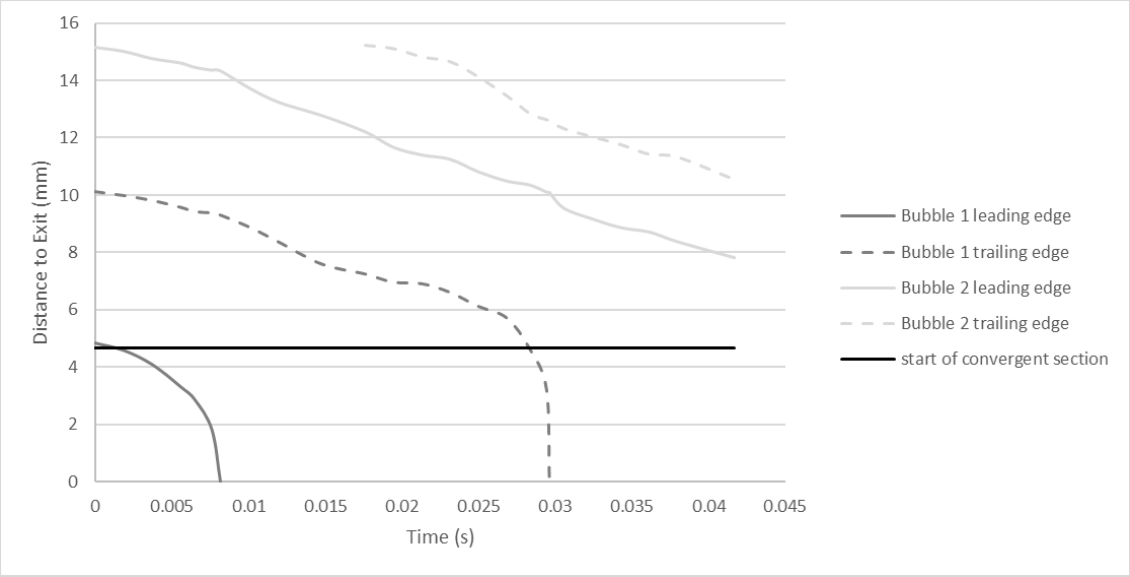


**FIGURE 12.** Experimental time trace of one big and small bubble (approximately 6 mm and 3 mm diameter sizes, respectively) leading and trailing edges

**1.2.** Impact of aspect ratio on drag and flow structure for cylinders with two free ends

Additionally, I spent a significant amount of time to perform both experimental and numerical works of aerodynamic drag study in a wind-tunnel setting during my Sabbatical. I participated heavily especially in wind-tunnel experiments as shown in Fig. 13, in studying the impact of aspect ratio on drag and flow structure for cylinders with two free ends using the wind tunnel facility at the University of St. Thomas. I worked with instrumentation that was set up with National Instruments (NI) data acquisition module and LabVIEW program. This research experience equipped me with many practical experimental techniques. It was found that cylinder drag depends more strongly on changes in aspect ratio in comparison to changes in Reynolds number (Re). An empirical relation is presented for use with cylinders having two free ends with AR = 2-15 and Re = 16,000-105,000 that shows good agreement with published data as well as the results in the current study. This empirical relation, when supplemented with historical data for an infinite cylinder, can be used to determine the drag coefficients within the limits. Numerical simulations demonstrate that the drag reduction of lower AR cylinders results from tip vortices increasing the pressure on the downstream part of the cylinder. This tip vortices are further found to persist downstream, though they can become increasingly distorted with increasing AR. Their presence reduces St magnitude in the wake as one moves towards the free end location from the midpoint. *A copy of the accepted peer-reviewed draft conference publication in the ASME FEDSM2022 proceeding is included in the appendix section*.

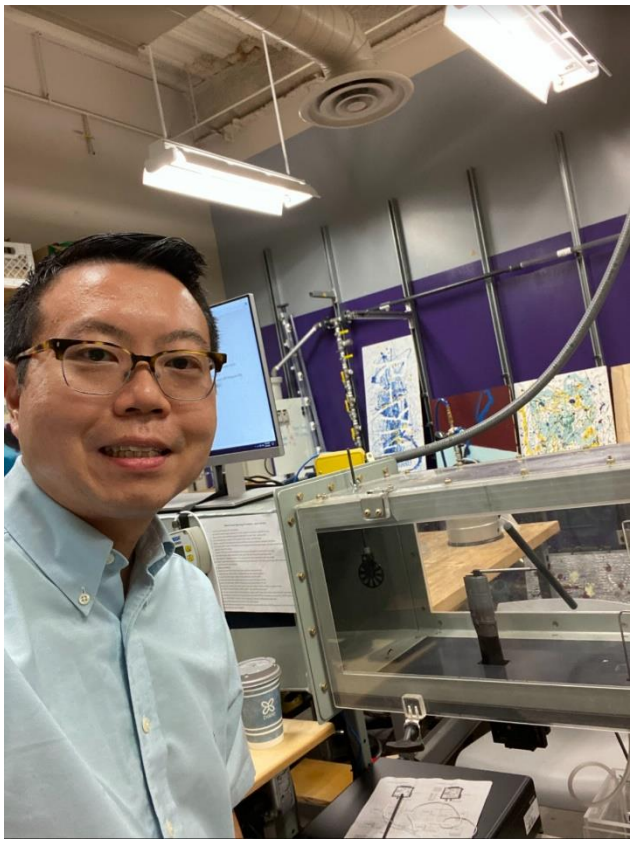

**Figure 13.** A snapshot of me working with the wind tunnel instrumentation and measurements at the University of St. Thomas, MN

**1.3.** Effect of bubble sizes and void fractions on thermal transport in homogeneous bubbly flow: Eulerian-Eulerian modeling

During my Sabbatical, I conducted numerical simulations using the Eulerian-Eulerian two-fluid model for convective heat transfer enhancement in a vertical rectangular bubble column with two focuses: the first being a validation of the Eulerian-Eulerian model with experimental data and the second being the finding of the optimum bubble diameter size for convective heat transfer. Bubbles with diameter sizes between 0.010-3.0mm at a velocity range between 0.275-0.325 m/s were injected into the column for the simulations. The inlet void fraction was varied in the range of 0.50-5.0% along with Rayleigh numbers in the range of $4.0\times10^{9}$ – $1.2\times10^{11}$. The results from the validation simulations were compared to the experimental data and these results validated the Eulerian-Eulerian model with the experimental data for simulating heat transport in homogeneous bubbly flow in a rectangular bubble column. The validation results also showed a significant heat transfer enhancement with the average Nusselt number proportional to void fraction with the power of ~0.45 and indicated that the average Nusselt number is nearly constant over Rayleigh numbers. The results from the simulation of different bubble diameters sizes at various average void fractions show that the Nusselt number increases with increasing void fraction, but the value does not consistently peak for one bubble size only. This research is currently a work in progress and a journal paper is under preparation to be submitted for publication.

**1.4.** Effect of a single nanoparticle diameter size on a nanochannel fluid flow and heat transfer

I worked with a Fresno State graduate student to employ a new simulation research paradigm, namely molecular dynamics (MD) simulation, to simulate the effect of a single nanoparticle diameter size on a nanochannel fluid flow and heat transfer during my Sabbatical. The MD simulation results are promising, particularly the fluid flow in a nanochannel setting. In the present work, a nanochannel with parallel copper walls and argon fluid atoms with flow conditions are investigated. Its aim is to observe behavior and convective heat transfer of nanofluid with a single spherical copper nanoparticle. Simulations were carried out by LAMMPS code, and all data is collected from their results. Velocity profiles show that adding a nanoparticle can increase the velocity, however, increasing the nanoparticle diameter does not necessarily mean the velocity increases. To examine the heat transfer, temperature profiles were observed. Results show that adding a single nanoparticle increases the temperature of the fluid closer to the inlet resulting in a lower heat transfer characteristic. The Nusselt number is also investigated to quantify the heat transfer characteristic of the system in comparison to base liquid. Results show that with an increase of diameter size of the nanoparticle, the Nusselt number can vary but typically increases which is due to the high temperature jump at the wall to the solid-like later of the fluid. *A copy of the accepted peer-reviewed draft conference publication in the ASME FEDSM2022 proceeding is included in the appendix section*.

**1.5.** A mitigation study of air treatment technology with a physical air filter on volatile organic compounds, carbon dioxide, and fine particulate matters generated by indoor smoke

I spent the remainder of my Sabbatical time to complete a funded indoor air quality (IAQ) research project. The research is to identify the best air treatment and filtration strategy to mitigate the volatile organic compounds (VOCs), fine particulate matters (PM), and carbon dioxide concentrations caused by a smoke contaminant source. Numerous combinations of filter (minimum efficiency reporting value or MERV and high efficiency particulate air filter or HEPA) and air treatment technology (Bipolar Ionizers (BPI) and UVC light) for assessing IAQ given an indoor space contaminated by a woodchip-based smoke source are tested. The primary goal of the research project is to evaluate the impact of using the BPI, if any, on mitigating the VOC, $CO_2$, and PM concentrations caused by the smoke contaminants. The secondary goal is to verify if a MERV filter combined with BPI technology can match the testing criteria or the performance of a HEPA filter. The research shows promising results. *A copy of the final report submitted to the ASHRAE San Joaquin Chapter is included in the appendix section*.

**Teaching**

**2.1.** Wind-tunnel National Instruments data acquisition and LabVIEW setup and instrumentation

I participated in conducting experimental drag measurements in a FLOTEK 1440 wind tunnel with a 30.48 cm x 30.48 cm x 91.44 cm test section at the University of St.

Thomas for the most part of my Sabbatical. The wind tunnel turbulence intensity measured as 1% of mean velocity with a hot-wire probe (TSI CTA-1750). Air speeds ranged from 10-30 m/s and were measured using a pitot-static probe (FlowKinetics P06-CF) connected to a differential pressure sensor (Dwyer 668B-05-3). The air density in the tunnel was determined by measuring the absolute pressure (Measurement Specialties US331-000005-015PA) and temperature (U.S. Sensor PR103J2). The average air density was 1.146 kg/m$^3$. A two-component dynamometer (Engineering Laboratory Design) was used for measuring drag. This system uses a strut assembly that is shrouded from the airstream and connected to a linear voltage differential transformer module. A calibration procedure was conducted before and after taking each experimental data point. While time consuming, this approach ensured that the calibration did not shift during data collection and allowed careful monitoring of drag uncertainty. Repeated measurements of all data were taken at a given flow condition for use in the uncertainty analysis whose results are summarized in Table 1. All instrumentation was set up with National Instruments (NI) data acquisition module and LabVIEW. Figure 14 shows a snapshot of LabVIEW front panel and block diagram whom I worked on during this Sabbatical. Figure 15 shows the National Instruments data acquisition system for the wind tunnel experimentation. I intend to bring the LabVIEW setup and instrumentation to mechanical engineering faculty at Fresno State who teach mechanical engineering laboratory courses because both research and industry sectors look highly upon it. Students will learn more about how to set up a NI data acquisition system and write a LabVIEW program from scratch to record pressure, velocity, and temperature measurements including the uncertainty analysis. My experimental work experience with NI data acquisition and LabVIEW setup during my sabbatical leave has the potential to enrich the laboratory teaching materials at Fresno State. In addition, it enables shifting the area of my academic emphasis from numerical to experimental techniques.

**TABLE 1:** AVERAGE MEASUREMENT UNCERTAINTY

| **Variable** | **Average Uncertainty (%)** |
|---|---|
| Drag Coefficient $C_D$ | 2.5 |
| Cylinder Diameter D | 0.1 |
| Cylinder Drag $F_c$ | 1.9 |
| Cylinder Length L | 0.1 |
| Free Stream Velocity $U_\infty$ | 0.6 |
| Air Density $\rho$ | 0.2 |
| Reynolds Number Re | 0.7 |

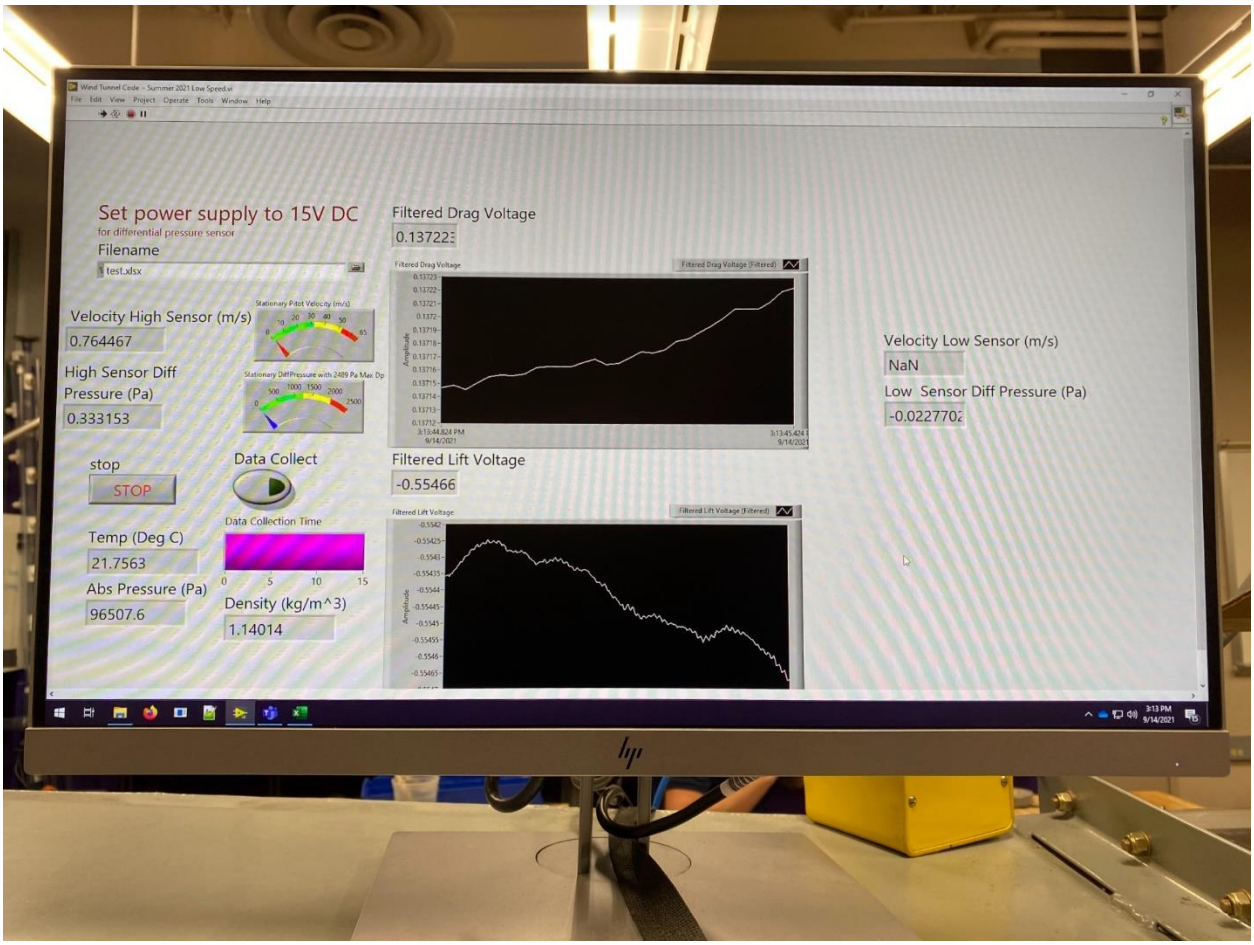


(a) LabVIEW front panel

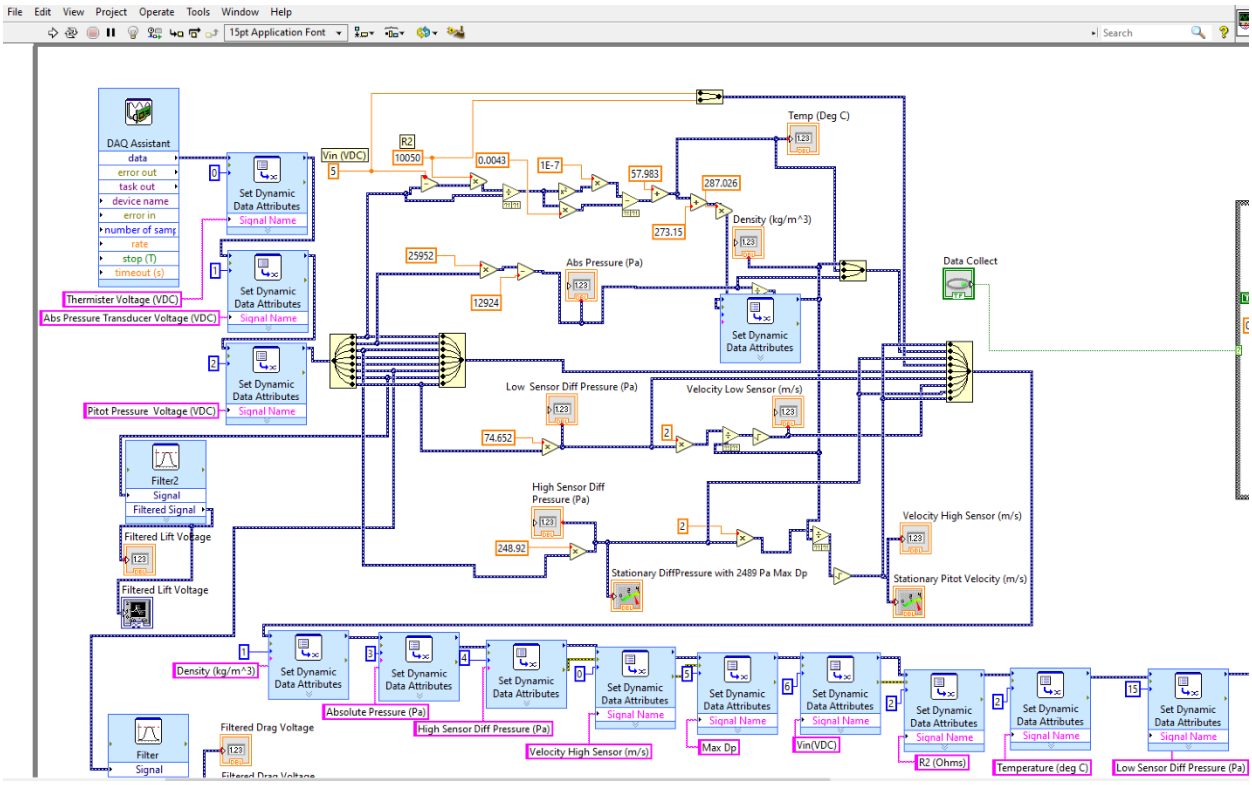


(b) LabVIEW block diagram

**Figure 14.** A snapshot of LabVIEW front panel and block diagram whom I worked for the wind tunnel experimentation during my sabbatical

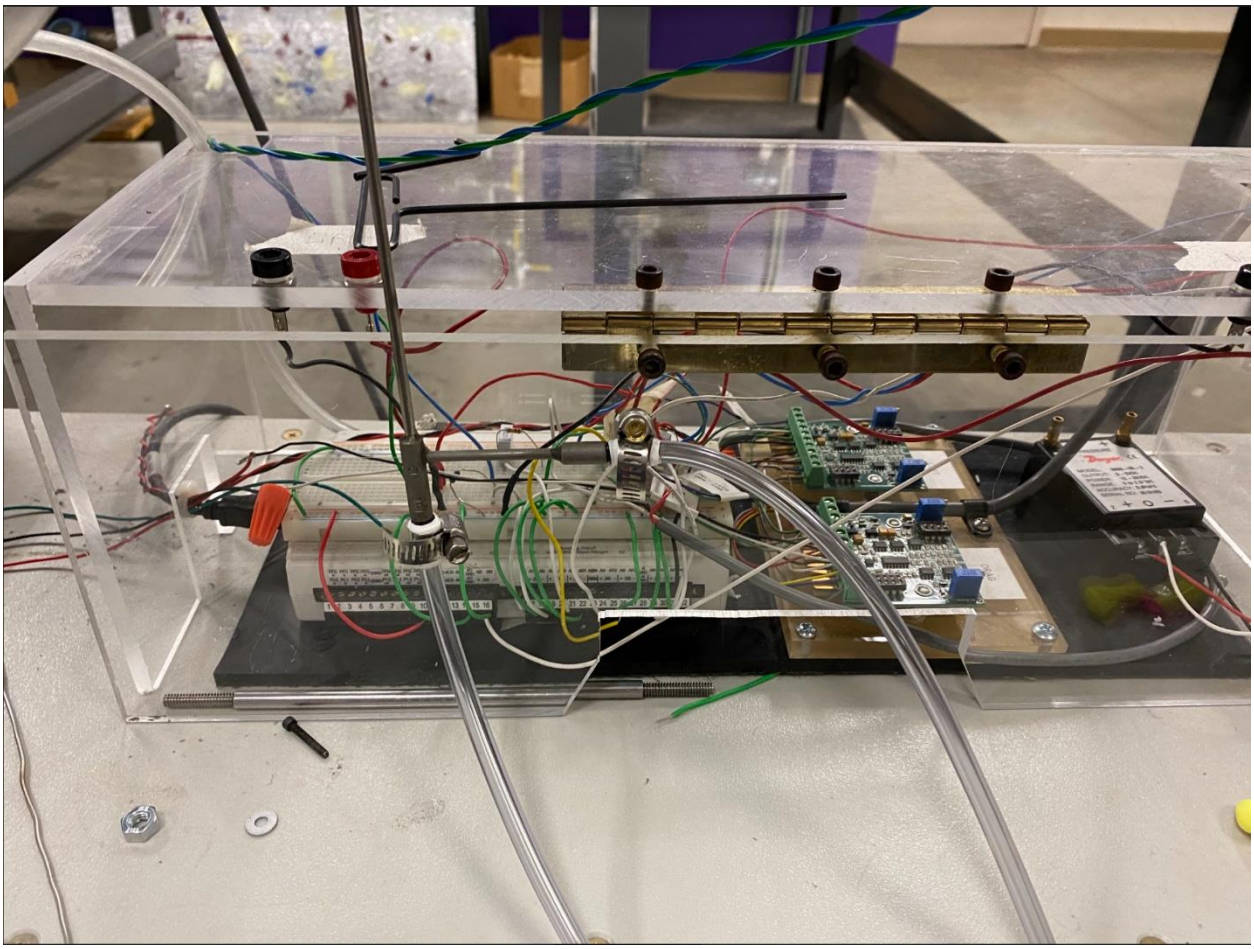

**Figure 15.** National Instruments data acquisition system for the wind tunnel experimentation

**2.2.** Thermo-fluid classroom and laboratory teaching observations

During my Sabbatical, I had the opportunity to observe all thermo-fluid lecture and laboratory classes at the University of St. Thomas. I attended both lecture and laboratory classes of ENGR 381 Thermodynamics (4 credits), ENGR 383 Fluid Mechanics (4 credits), and ENGR 384 Heat Transfer (4 credits). An important takeaway I had is all their thermo-fluid courses include laboratory components in the curriculum, so it makes up 4 credits (approximately 3 credits for lecture and 1 credit for laboratory) for each mentioned course. An inclusion of laboratory components strengthens the thermo-fluid courses because it provides strong practical and hands-on learning experiences for students. For example, we do not have thermodynamics laboratory and heat transfer laboratory classes in the mechanical engineering curriculum at Fresno State currently. I think the laboratory components embedded in both thermodynamic and heat transfer courses are what we are missing, and we probably can learn from the University of St. Thomas to apply those laboratory materials to our curriculum. Figure 16 shows a snapshot of the ENGR 383 Fluid Mechanics lecture in person. The pedagogy of the fluid mechanics instructor was considered organized. The instructor started the lecture with class announcements followed by a review of last lecture material, iClicker questions, and a full presentation of new lecture material for each

class period. Additionally, the instructor recorded all lectures using Zoom recording throughout the semester. Passion and patience are two outstanding teaching attributes I observed from this fluid mechanics instructor. Majority of the class students are white (Caucasian) followed by Asian and Latino/Hispanic ethnicities. In that fluid mechanics class, approximately 25% are female students. Most of the thermo-fluid tenured faculty received their doctoral degrees in mechanical engineering from the University of Minnesota, Twin-Cities, which is situated right across from the campus of the University of St. Thomas over the Mississippi River.

**Figure 16.** A snapshot of the ENGR 383 fluid mechanics lecture

**Summary**

In summary, this Sabbatical expanded my research and teaching capacity in the field of fluid mechanics. I had the opportunity to work alongside a tenured experimental fluid mechanics faculty in conducting a two-phase bubbly flow experiment using a high-speed camera and performing wind-tunnel experiments using a National Instruments data acquisition module and a LabVIEW program. While performing experiments on-site, I developed my skills on experimental techniques because my original academic emphasis is in the field of numerical computations (*a shift in areas of academic*

*emphasis*). This Sabbatical gave me time in completing the work of the validation of the Eulerian-Eulerian models with a published bubbly flow and heat transfer enhancement experiment and determining the optimal bubble diameter size and void fraction in enhancing a two-phase air-water flow system. Sabbatical products include two peer-reviewed conference publications and one technical report publication. Both peer-reviewed conference publications are in the areas of aerodynamic drag and nano thermo-fluid, respectively. The technical report publication is a product of the experimental study of indoor air quality conducted during this Sabbatical.

This Sabbatical had a tremendous impact on my research and teaching in the field of fluid mechanics and I envision benefiting the Mechanical Engineering Department and the Lyles College of Engineering in terms of continuously improving my pedagogy and building the state-of-the-art fluid mechanics laboratory facility, for example, *the National Instruments and LabVIEW instrumentation setup*. I plan to upgrade our wind-tunnel instrumentation setup at Fresno State to allow longer data-logging time and to provide real-time monitoring capability. Most importantly, it provides an in-house low-cost instrumentation setup. This Sabbatical benefited my fluid mechanics (ME 116) and fluid mechanics laboratory (ME 118) course instructions and pedagogy. Finally yet important, this Sabbatical benefited the University by representing Fresno State for conducting research and sharing best practices in teaching with faculty from the University of St. Thomas, MN.

## APPENDIX:

**Proceedings of the ASME 2022**
**Fluids Engineering Division Summer Meeting**
**FEDSM2022**
**August 1-3, 2022, Toronto, Ontario, Canada**

**FEDSM2022-87706**

# IMPACT OF ASPECT RATIO ON DRAG AND FLOW STRUCTURE FOR CYLINDERS WITH TWO FREE ENDS

**Thomas Shepard**
University of St. Thomas
Saint Paul, MN

**Deify Law**
California State University, Fresno
Fresno, CA

**Jacob Dahl**
University of St. Thomas
Saint Paul, MN

**Rhett Reichstadt**
University of St. Thomas
Saint Paul, MN

**Arun Sriniwas Selvamani**
California State University, Fresno
Fresno, CA

## ABSTRACT

*When examining the literature for flow effects on circular cylinders one can find many studies on infinite cylinders and cantilevered cylinders but minimal data related to cylinders with two free ends. The limited data available shows that the cylinder aspect ratio affects the drag and frequency content of flow within the wake however these studies were done at discreet Reynolds numbers. In order to better understand the combined impact of aspect ratio and Reynolds number a series of wind tunnel tests and numerical simulations has been conducted for cylinders with two free ends having aspect ratios of 2-15. Test were conducted in the subcritical regime with Reynolds numbers ranging 9300 - 105,000. Tip vortex effects, which vary with aspect ratio, are shown to impact the cylinder surface pressure, drag coefficient and wake Strouhal numbers though Reynolds number effects are minor for the conditions studied. The results are compared against existing historical data and show the trend of drag coefficient increasing with cylinder aspect ratio.*

Keywords: cylinder, tip vortex, drag coefficient, Strouhal number

## NOMENCLATURE

| | |
|---|---|
| AR | cylinder aspect ratio (L/D) |
| $C_D$ | drag coefficient of cylinder with two free ends |
| $C_{D\infty}$ | drag coefficient of infinite cylinder |
| D | cylinder diameter |
| $F_c$ | cylinder drag force |
| L | cylinder length |
| Re | Reynolds number |
| St | Strouhal number |
| $U_\infty$ | air free stream velocity |
| $\kappa$ | drag coefficient reduction factor |
| $\rho$ | air density |
| $\mu$ | dynamic viscosity |

## 1. INTRODUCTION

Due to the prevalence of circular cylinders in numerous applications, much is known about the forces and flow features that develop when the cylinder experiences a flow normal to its axis. However, it is important to note that the end conditions of the cylinder play a role. Thus, one may break the topic of flow around a cylinder into different subsets such as : infinite cylinders, cantilevered cylinders (one free end), surface piercing cylinders involving a gas/liquid interface, and cylinders with two free ends.

The canonical work on cylinder drag was conducted by Wieselsberger [1] which resulted in the $C_D$ vs. Re plot that is commonly found in fluid mechanics textbooks for smooth circular cylinders. This plot is applicable for infinite cylinders, or cylinders of sufficient length such that the tip vortices forming at the free ends of the cylinder have an insignificant effect on the macroscale flow features. It is noted that the infinite cylinders used in [1] had aspect ratios (AR = L/D) of 280 and greater, or had the ends of the cylinder very near a flat wall so that tip vortices would not form.

While the infinite cylinder has been studied extensively, there have been relatively few studies on cylinders with two free ends. However, better knowledge of drag on cylinders with two free ends would be of relevance in many areas including cranes lifting materials on construction sites, tethered loads beneath

helicopters, cylinders free falling in the ocean and storm blown debris. Wieselsberger investigate d the $C_D$ vs. Re relationship for an AR 5 cylinder[2] finding that the finite length cylinder has a lower drag coefficient in the subcritical Reynolds regime ($Re < 2 \times 10^5$). The effect of varying aspect ratio on drag coefficient was examined at a Reynolds of 88,000 for AR = 1, 2, 3, 5, 10, 20, 40 and infinite. The results show that decreasing AR continued to decrease $C_D$.

Zdravkovich et al. studied flow around cylinder with two free ends with AR = 2-10 [3]. Their AR = 5 Cd data was found to be somewhat higher than that o f Wieselsberger when compared over the Re range of ~70,000 -160,000. Additionally, for this Re range it was reported that AR 2 cylinder had a slightly higher CD than an AR 3 cylinder, a result that is different than Wieselsberger. However, the general trend of decreasing AR resulting in a lower Cd was confirmed though it was conclude d that decreasing AR below 5 produced minimal reductions in drag coefficient. The physical explanation for the reduced drag was presented as a higher pressure on the back of the body caused by flow into the wake region near the free ends. This three - dimensional flow causes differences in the wake of the cylinder in comparison to the flow behind an infinite cylinder. It was found that having two free ends allows for interacting tip flows that can inhibit vortex shedding . Hot wire measurements were used to reveal irregular vortex shedding behind the AR 2 -8 cylinders with Strouhal numbers ranging from 0.14 -0.25.

Recently, Potts et al. [4] conducted experiments for comparison against current design guidance related to cylinders with free ends provided in [5]. The design guidance employs a drag coefficient reduction factor ( $\kappa$) and historical data for an infinite cylinder to determine drag from a cylinder with two free ends as shown in Equation 1.

$$\kappa = \frac{C_D}{C_{D\infty}} \qquad (1)$$

It is concluded that the design guidance in [5] likely stemmed from Wieselsberger data [2] and Potts et al. provide their own results as shown in Table 1. The correction factors shown in Table 1 are specific to cylinders with two free ends though Potts et al. also provide reduction factors for cylinders with one free end. While the results are suggested for subcritical Reynolds numbers the impact of Reynolds number on the drag coefficient reduction factor was not explored.

**TABLE 1:** DRAG COEFFICIENT REDUCTION FACTORS

| **AR** | **K** [2] | **K** [4] | **K** [5] |
|---|---|---|---|
| 2 | 28.6 | 0.54 | 0.58 |
| 5 | 28.6 | 0.62 | 0.62 |
| 10 | 28.6 | 0.69 | 0.68 |
| 20 | 22.2 | 0.77 | 0.74 |
| 40 | 15.9 | 0.85 | 0.82 |

The effect of reducing $C_D$ with reducing AR seems to occur in the subcritical Reynolds region and disappear in the supercritical regime. This is shown by Wieselsberger [2] and Xiang and Soares [6] for an AR 5 cylinder[2] and by Prosser and Smith [7] for AR 1 and 2 cylinders. The data collapses onto the trend line of an infinite cylinder. However, there is some disagreement on this. Gao et al. [8] ran simulations on an AR 1.5 cylinder for the Reynolds range of $4.6$-$10^6$. Their simulations did not show a characteristic dip in $C_D$ as Re increased to demark the transition to supercritical conditions.

The tip vortex that forms from a cylinder free end has been studied extensively for wall mounted (cantilevered) cylinders, for example [9-12]. Sumner provides a review of the lit erature prior to 2013 [13] detailing the counter -rotating vortices tha t form at the cylinder free end, the horseshoe vortex that forms at the cylinder base and their effects on $C_D$ and vortex shedding at various AR. While this geometry shares similarities with a two free end cylinder there are also significant differences that affect the flow. Gao et al.[8] simulated flow around cylinders with two free ends having AR 1 -5 and Re of 45, 450, and 45,000. They find that increasing Re leads to unsteadiness in the wake region though four spiral vortices are identified as have a swing imparted similar to that of a von Kármán vortex sheet. For AR < 6 it is argued that the shape of the free ends effects the tip vortex inflow in the cylinder wake, effectively limiting its impact on drag force modification.

Upon reviewing the limited literature one finds gaps related to the effect that Re can play on drag coefficient for cylinders with two free ends as well as the effect of changing AR on wake features. One also finds some results that are inconsistent. The current study was motivated to help fill some of these gaps and develop a more complete understanding of the effects that AR and Re play for subcritical flow around cylinders with two free ends. In this paper a series of wind tunnel experiments are done for a range of AR and Reynolds numbers.Numerical simulations were also conducted for the range of AR studied experimentally to further elucidate why the drag force is modified by changing AR and how the flow features are impacted.

## 1. MATERIALS AND METHODS

### 2.1 Experimental Methods

The physical cylinders of varying aspect ratios (2-15) used in this study were made of Delrin. The dimensions of the cylinders are provided in Table 2 in addition to their blockage of the wind tunnel test section. The drag coefficient data presented here have been corrected to account for blockage using Maskell's Theory as presented in [14]. These corrections ranged from 1.2 - 4.3% reductions in the measured drag coefficients. The wind tunnel (FLOTEK 1440) test section had a cross section area of 30.48 cm x 30.48 cm. During testing the wind speed was varied from ~ 9-59 m/s as measured via a pitot-static probe (FlowKinetics P06-CF with differential pressure sensor Dwyer 668B-05-3). Air density in the wind tunnel was found by recording the absolute pressure and temperature in the test section (Measurement Specialties US331 -000005-015PA, U.S. Sensor PR103J2). Air viscosity was determined using the

measured temperature with Sutherland's Law. The Reynolds numbers covered were 9300-105,000.

**TABLE 2:** CYLINDER DIMENSIONS

| AR | D (mm) | L (mm) | Blockage (%) |
|---|---|---|---|
| 2 | 28.6 | 57.2 | 1.8 |
| 3 | 28.6 | 85.7 | 2.6 |
| 5 | 28.6 | 142.9 | 4.4 |
| 10 | 22.2 | 222.3 | 5.3 |
| 15 | 15.9 | 238.1 | 4.1 |

Cylinders were mounted as shown in Fig. 1 and drag force was measured via a two-component dynamometer incorporating a linear voltage differential transformer (Engineering Laboratory Design). The dynamometer was calibrated both before and after each drag measurement to ensure that calibration did not shift during operation allowing for careful oversight over drag measurement uncertainty. During testing, measurements were taking for 10 -20 seconds and the results were aver aged. The average uncertainties for experimental measurements are provided in Table 2.

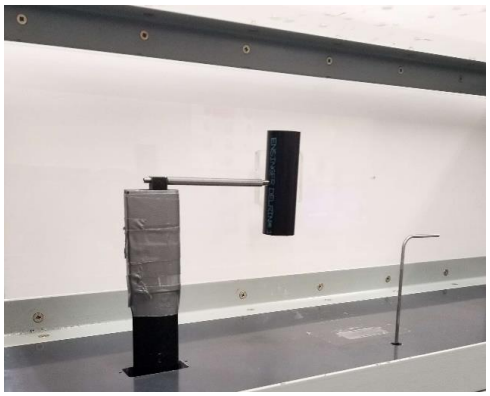

**FIGURE 1:** AR 3 CYLINDER MOUNTED IN WIND TUNNEL

**TABLE 2:** AVERAGE MEASUREMENT UNCERTAINTY

| Variable | Average Uncertainty (%) |
|---|---|
| $C_D$ | 2.5 |
| D | 0.1 |
| $F_c$ | 1.9 |
| L | 0.1 |
| $U_\infty$ | 0.6 |
| $\rho$ | 0.2 |
| Re | 0.7 |

### 2.2 Numerical Methods

Computational fluid dynamics (CFD) simulations were conducted at the CFD Laboratory of Fresno State using the commercial software ANSYS Fluent (2021) in this present work. The ANSYS Fluent (2021) is based on the finite volume time integration method. The semi-implicit method for pressure-linked equations (SIMPLE) algorithm was employed for the incompressible airflow in the simulations. A 0.000001 s time step size with 100 sub iterations was used to advance the transient solutions from 0 to 2 s numerically. Results were time averaged from 1 to 2 s. The boundaries of the computational domain were treated as symmetry boundary conditions whereas the rest used velocity and pressure boundary conditions for inlet and outlet of the flow domain, respectively. Inlet turbulence kinetic energy and dissipation rate boundary conditions were specified based on turbulence intensity of 1.1% and hydraulic diameter for all cases. All dependent variables were specified with a convergence criterion of $1\times10^{-8}$. The cylinder with two free ends is situated at the lengthwise center of the flow domain. Large eddy simulation with the Smagorinsky-Lilly subgrid-scale model was employed to compute the turbulent viscosity in the present work. In addition, a grid-independent solution was attained, and the optimal number of grids required for a convergent solution was found to be at least 8 million meshes. Cylinder shape component's surface y+ values were ensured to be around 1.0 by refining mesh near the surface.

## 1. RESULTS AND DISCUSSION

The wind tunnel testing resulted in 45 different operating conditions being tested. The Reynolds range available for each cylinder was determined by the following factors: cylinder diameter, maximum wind tunnel speed, minimum drag force that could be accurately measured. Simulations were conducted at Re = 45,000 for the five different AR cylinders. In comparing the simulated drag coefficients with the experimental data an average deviation of ± 2.4% was found. This agreement falls within the experimental uncertainty. The simulation results were further compared against data from Gao et al. [8] who used the Shear-Stress Transport (SST) Scale-Adaptive Simulation (SAS) model to simulate a flow over a cylinder with two free ends. With an aspect ratio of 5, [8] predicted found $C_D = 0.75$, while for similar conditions numerical methods used here found $C_D = 0.77$. These comparisons against data from multiple sources provides confidence in the validity of the numerical methods used. Below we detail the results starting with experiments and followed by simulations.

Figure 2 shows the relationship between cylinder drag coefficient, Reynolds number and AR. For a given cylinder there was scatter in the data as Re was varied. This result was confirmed with repeated trials. While the general trend of increasing AR resulting in a lower $C_D$ was confirmed, the data show that for AR 2-5 this is not always the case. These results are consistent with the experimental data in [3]. For a given AR, the variation in CD found with Re averaged 5.3% which is above the measurement uncertainty. For the same Re range it is noted that Wieselsberger AR 5 data [2] shows a $C_D$ variation of 5%. Quantifying and confirming the scatter in the data is useful from a design perspective for understanding the tolerances to apply when using empirical results.

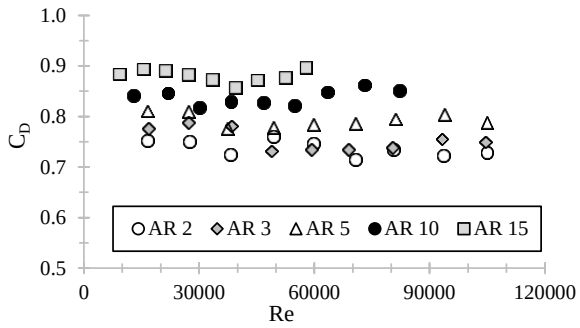


**FIGURE 2:** TWO FREE END CYLINDER DRAG DEPENDENCE ON REYNOLDS NUMBER AND ASPECT RATIO

The experimental data was converted into drag coefficient reduction factors using [2] as the source of the infinite cylinder drag coefficient at a given Reynolds number. While small, casting the data in this format reveals a trend of decreasing drag reduction ratio for increasing Reynolds number on average. In comparison to the data in Fig. 2, the data in Fig. 3 shows an increase in the relative amount of variation found for a given cylinder as Re is varied (8.6%). The AR 15, Re 9300 trial is shown to give a drag reduction factor that is much higher than those at higher Re. This is largely due to the fact that the infinite cylinder drag coefficient trend is roughly constant for Re = 16,000 – 176,000 but starts to dip when Re is reduced from 16,000 towards 1400. This suggests that the practical use of drag reduction ratios, if they are to be considered as constant over a Re range, should be restricted to subcritical Reynolds numbers above 16,000.

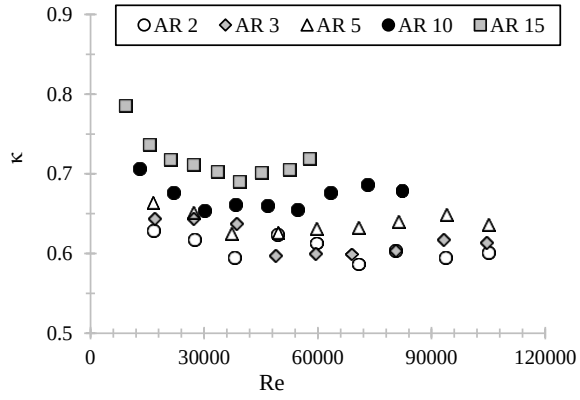


**FIGURE 3:** DRAG REDUCTION RATIO DEPENDENCE ON REYNOLDS NUMBER AND ASPECT RATIO

As demonstrated in Figs.2-3, the Reynolds effect on drag is small for the range of Re and AR considered. In order to compare our results more easily against published literature we calculated the average drag reduction ratio for a given AR with the results presented in Fig. 4. The data shows good agreement between studies for AR 10-20 but shows significant scatter for AR 5 and lower. Whereas some studies have suggested that AR reductions below 5 would lead to minimal reductions in drag [3,8], the universality of that conclusion may be premature. These inter-study variations at low aspect ratio provide motivation for future studies.

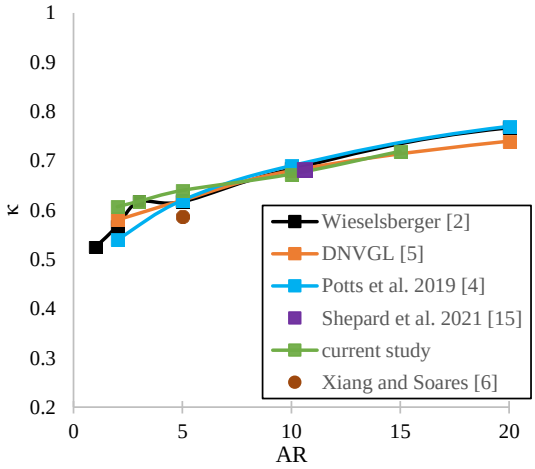


**FIGURE 4:** COMPARISON OF DRAG REDUCTION RATIO DEPENDENCE ON ASPECT RATIO FROM PUBLISHED LITERATURE

The data in Fig. 3 were curve fit in order to arrive at an empirical relationship that would allow AR and Re to be used to determine the drag coefficient reduction ratio. Equation 2 captures the trends found in the experimental data with an average deviation between equation and experiment of 1.8%. When Equation 2 is compared against the Wieselsberger AR 5 data for Re of 40,700-108,400 the average deviation is 2.5%. We note that Potts et al. [4] present a similar equation for finding the drag coefficient reduction factor based solely on AR by applying a curve fit to the Wieselsberger data of varying AR at Re = 88,000. The utility of Equation 2 presented here lies in its development using a larger data set, its verification against published literature and having expressed limits: AR = 2-15, Re = 16,000-105,000. The utility of the Potts et al. relationship is in that it covers a larger range of AR.

$$\kappa = 0.78 \cdot AR^{0.07064} \cdot Re^{-0.028} \quad (2)$$

In order to better understand the reason for drag coefficients to reduce with increasing AR numerical simulations were conducted to identify the surface pressures on the cylinders. Figure 5 shows the front view of simulated time-averaged normalized pressure on cylinder surface of increasing aspect ratio for Re = 45,000. The static pressure on a cylinder surface is normalized by its corresponding stagnation pressure. The highest normalized pressure concentrates uniformly near the

leading edge except for AR 10, which is slightly scattered. Figure 6 shows the back view of simulated time-averaged normalized pressure on cylinder surface of increasing aspect ratio. It is found that vacuum pressure increases near the free ends of cylinder as the aspect ratio of a cylinder increases. A greater vacuum pressure enhances drag of a cylinder with a higher aspect ratio. Both findings of Figs. 5 and 6 are consistent with the work of Shepard et al. [15].

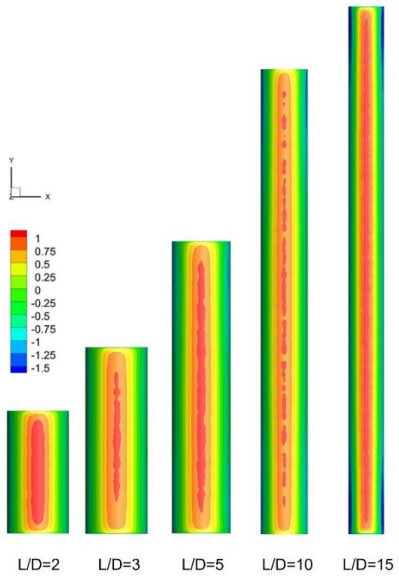


**FIGURE 5:** FRONT VIEW OF SIMULATED TIME-AVERAGED NORMALIZED PRESSURE ON CYLINDER SURFACE OF INCREASING ASPECT RATIO FOR *Re* = 45,000

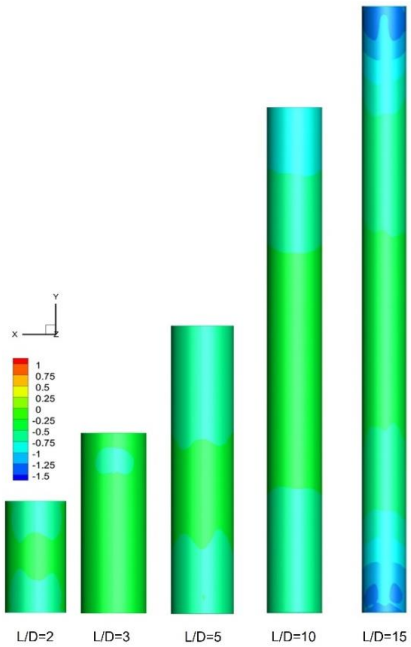


**FIGURE 6:** BACK VIEW OF SIMULATED TIME-AVERAGED NORMALIZED PRESSURE ON CYLINDER SURFACE OF INCREASING ASPECT RATIO FOR *Re* = 45,000

Figure 7 presents the simulated cylinder drag coefficient dependence on position along the normalized cylinder length and aspect ratio for Re = 45,000. The predicted rising followed by falling trend of drag coefficient from the tip towards the center of cylinder is generally consistent with the work of Potts et al. [4]. The rising and falling trend of the drag coefficient is not profound when the aspect ratio is lower such as 2 and 3. This suggests that the effects of the tip vortices are felt along the entire length of the shorter cylinders. However in Fig. 7 one notes the relatively flat profiles of $C_D$ for AR 5-15 around the midpoint of the cylinder suggesting that the tip effects have not yet reached the middle of the cylinder.

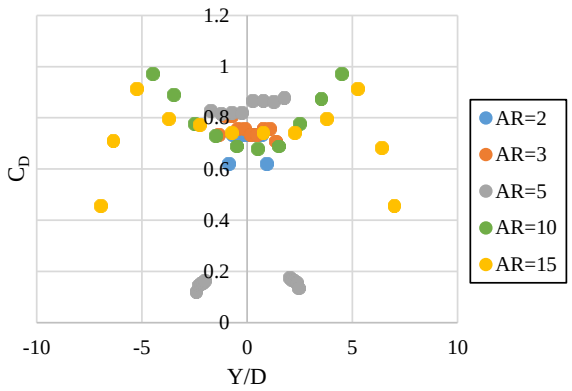


**FIGURE 7:** SIMULATED TWO FREE END CYLINDER DRAG COEFFICIENT DEPENDENCE ALONG NORMALIZED CYLINDER LENGTH (L) AND ASPECT RATIO FOR *Re* = 45,000

The simulated time-averaged streamwise velocity fields are shown in Fig. 8. The velocity fields are given as a sideview for a vertical plane on the cylinder centerline for varying AR. The streamwise velocity is normalized by its corresponding free stream velocity. Tip vortices create a downwash and upwash in the flow near the upper and lower free ends of the cylinder, respectively. This causes a low velocity field region that extends multiple diameters downstream of the cylinder. Xiang and Soares [6] have presented similar results for an AR 5 cylinder in comparison to an infinite cylinder whose low velocity region extends downstream less than one diameter for Re = 20,000. Results indicate that the low velocity region extends further downstream from the cylinder as aspect ratio increases.

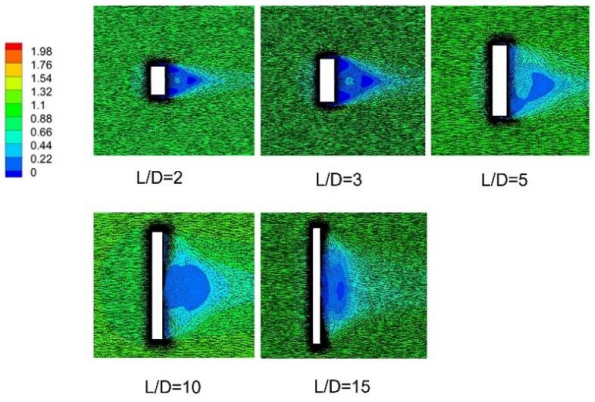


**FIGURE 8:** SIMULATED TIME-AVERAGED STREAMWISE VELOCITY FIELD IN VERTICAL PLANE ON BODY CENTERLINE (SIDE VIEW) FOR *Re* = 45,000 ON CYLINDER OF INCREASING ASPECT RATIO. COLOR SCALE IS NORMALIZED STREAMWISE VELOCITY ($u/U_\infty$).

Figure 9 presents the time-averaged nondimensional streamwise wake vorticity field in plane normal to free stream 6D downstream of cylinder for increasing AR. At lower aspect ratios of 2 and 3, counter-rotating circular vortex pairs formed in the vicinity of both free ends of the cylinder are observed to show strong symmetry. The counter-rotating vortex pair shapes becomes distorted and elongated in the cylinder axis direction as aspect ratio increases. It is shown that downstream from the cylinder these tip vortices can extend to the cylinder midline which would affect the formation and propagation of von Kármán sheet vortices from the cylinder. The simulated streamwise wake vorticity patterns behind a cylinder free end shown in Fig. 9 are consistent with [13, 15]. The aspect ratio appears to have little effect on the vorticity magnitude which may be more impacted by changes in Reynolds number.

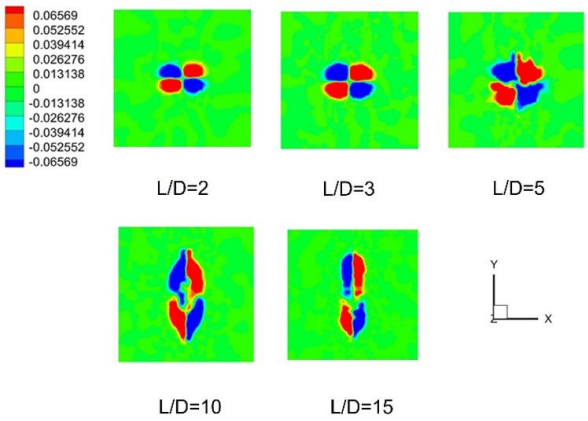


**FIGURE 9:** SIMULATED TIME-AVERAGED NONDIMENSIONAL STREAMWISE WAKE VORTICITY FIELD IN PLANE NORMAL TO FREE STREAM 6*D* DOWNSTREAM OF CYLINDER OF INCREASING ASPECT RATIO FOR *Re* = 45,000

Figure 10 shows the simulated Strouhal number dependence on position along the normalized cylinder length for varying aspect ratios. The Strouhal number results were taken 2.5D downstream from the cylinder midpoint and 1D offset from the spanwise direction. It is noted that the ability to detect frequency peaks was sensitive to position and that the amplitude of the frequency peaks in an FFT were smaller for smaller aspect ratio cylinders and closer to the free end positions. The three dimensionality of the tip vortices interfering with sheet vortex formation has been noted by most authors who report Strouhal data behind finite cylinders [3, 4, 6, 8]. The data in Fig. 10 show the Strouhal number is reduced near the free end providing further evidence of tip vortices modifying flow in comparison to an infinite cylinder. This trend has also been found in cantilevered cylinders, see for example [4, 13]. The predicted Strouhal number near the center of the cylinder ranges from 0.15 to 0.19. A consistent trend is not found correlating aspect ratio with peak Strouhal number. However, lower aspect ratio cylinders are found to experience a continuous gradient in St

when moving from the free end towards the midpoint of the cylinder within the wake.

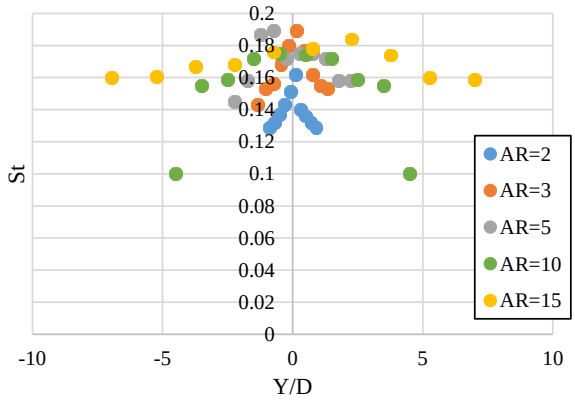


**FIGURE 10:** SIMULATED TWO FREE END CYLINDER STROUHAL NUMBER DEPENDENCE ALONG NORMALIZED CYLINDER LENGTH (L) AND ASPECT RATIO FOR *Re* = 45,000

## 4. CONCLUSIONS

Through wind tunnel experiments and numerical simulations this work has investigated how drag and flow characteristics are affected by changes in Re and AR for cylinders with two free ends. It was found that cylinder drag depends more strongly on changes in aspect ratio in comparison to changes in Re. An empirical relation is presented for use with cylinders having two free ends with AR = 2-15 and Re = 16,000-105,000 that shows good agreement with published data as well as the results in the current study. This equation, when supplemented with historical data for an infinite cylinder [2], can be used to determine the drag coefficients within the aforementioned limits. Numerical simulations demonstrate that the drag reduction of lower AR cylinders results from tip vortices increasing the pressure on the downstream part of the cylinder. This tip vortices are further found to persist downstream, though they can become increasingly distorted with increasing AR. Their presence reduces St magnitude in the wake as one moves towards the free end location from the midpoint.

## REFERENCES

[1] Wieselsberger, C., *New data on the laws of fluid resistance*. No. NACA-TN-84. 1922.

[2] Prandtl, L., Wieselsberger, C., and Betz, A., 2009, *Ergebnisse der aerodynamischen Versuchsanstalt zu Göttingen*. No. 5, Universitätsverlag Göttingen.

[3]Zdravkovich, M.M., Brand, V.P., Mathew, G., and Weston, A., 1989, "Flow past short circular cylinders with two free ends," *Journal of fluid mechanics*, 203, pp. 557-575.

[4] Potts, D.A., Binns, J.R. Potts, A.E., and Marcollo, H., 2019, "The effect of aspect ratio on the drag of bare cylinders." Proceedings of the International Conference on Offshore Mechanics and Arctic Engineering, ASME Paper No. OMAE2019-96431.

[5] DNV GL AS, 2014, "Environmental Conditions and Environmental Loads," DNV Technical Paper Recommended Practice DNV-RP-C205.

[6] Xiang, G. and Soares, C.G., 2020, "Improved dynamical modelling of freely falling underwater cylinder based on CFD," *Ocean Engineering*, 211, 107538.

[7] Prosser, D. and Smith, M., 2015, "Aerodynamics of finite cylinders in quasi-steady flow," Proceedings of the 53rd AIAA Aerospace Sciences Meeting, Paper No. 1931.

[8] Gao, W., Nelias, D., Liu, Z. and Lyu, Y., 2018, "Numerical investigation of flow around one finite circular cylinder with two free ends," *Ocean Engineering*, 156, pp. 373-380.

[9] Sumner, D., Heseltine, J.L., Dansereau. O.J.P., 2004, "Wake structure of a finite circular cylinder of small aspect ratio," *Experiments in Fluids*, 37, pp. 720-730.

[10] Okamoto, S., Sunabashiri, Y., 1992, "Vortex shedding from a circular cylinder of finite length placed on a ground plate," *ASME Journal of Fluids Engineering*, 114, pp. 512-521.

[11] Okamoto, T. and Yagita, M., 1973, "The experimental investigation on the flow past a circular cylinder of finite length placed normal to the plane surface in a uniform stream," *Bulletin of JSME*, 16(95), pp.805-814.

[12] Farivar, D., 1981, "Turbulent Uniform Flow around Cylinders or Finite Length," AIAA Journal, 19(3), pp. 275-281.

[13] Sumner, D., 2013, "Flow above the free end of a surface-mounted finite-height circular cylinder: A review," Journal of Fluids and Structures, 43, pp. 41-63.

[14] Anthoine, J., D. Olivari, and D. Portugaels., 2009, "Wind-tunnel blockage effect on drag coefficient of circular cylinders." *Wind & structures*, 12(6), pp. 541-551.

[15] Shepard, T. G., Law, D., Menon, R. K., Ordahl, K., and Gutenberg, A., 2021, "Interference drag and flow structure around cylinder-sphere junction," *Ocean Engineering*, 234, 109276.

**Proceedings of the ASME 2022**
**Fluids Engineering Division Summer Meeting**
**FEDSM2022**
**August 1-3, 2022, Toronto, Ontario, Canada**

# FEDSM2022-86966

## EFFECT OF SINGLE NANOPARTICLE DIAMETER SIZE ON A NANOCHANNEL FLUID FLOW AND HEAT TRANSFER

**Isaias Gonzalez**
California State University, Fresno
Fresno, CA

**Deify Law**
California State University, Fresno
Fresno, CA

## ABSTRACT

*This present work studies the effect of single nanoparticle diameter size on a nanochannel fluid flow and convective heat transfer using the molecular dynamics simulation code LAMMPS. The channel dimensions are 95 Å in length, 40 Å in depth, and 60 Å in height. Channel wall temperatures are fixed at 200 K whereas inlet bulk fluid temperature is set as 300 K. Two regions (force region and thermostat region) are considered before the channel inlet to create a flow and apply the quasi-periodic boundary condition to the system. Fluid and solid (walls and nanoparticle) materials are argon and copper, respectively. Surface wettability are modeled by setting the energy scale to be 1.67 x $10^{-21}$ J and the input force is imposed at 0.002 eV/Å. Both velocity and temperature profiles across the channel height will be plotted at 12.5, 22.5, and 32.5 Å away from the inlet. Effect of single nanoparticle diameter of 0.8, 1.0, 1.25, 1.5, 1.75, and 2 nm on the convective heat transfer enhancement will be studied. Nusselt number will be used to quantify the convective heat transfer enhancement with the presence of a nanoparticle size in the nanochannel flow. Nusselt number of a base nanochannel fluid flow without any nanoparticle will be included as a benchmark comparison.*

Keywords: molecular dynamics, nanoparticle, nanochannel, Nusselt number, Poiseuille flow, convective heat transfer

## NOMENCLATURE

| | |
|---|---|
| Ar | argon atom |
| Cu | copper atom |
| D | nanoparticle diameter (Å) |
| $F_i$ | embedding energy of atom *i* |
| h | heat transfer coefficient |
| k | thermal conductivity |
| L | channel width |
| $k_b$ | Boltzmann constant |
| $m_j$ | atom mass of atom *j* |
| n | number of bins |
| N | number of atoms |
| Nu | Nusselt number |
| $R_{ij}$ | distance between atoms *i* and *j* |
| T | temperature (K) |
| $T_b$ | bulk temperature (K) |
| $T_w$ | wall temperature (K) |
| U | EAM potential |
| $V_{ave}$ | center of mass velocity |
| $V_j$ | velocity of atom *j* |
| $V_x$ | velocity in *x* direction |

### GREEK SYMBOLS

| | |
|---|---|
| $\Delta$ | gradient operator |
| $\varepsilon$ | energy parameter |
| $\rho$ | fluid density |
| $\sigma$ | length scale |
| $\Phi$ | potential energy |
| $\Phi_w$ | wall potential energy |
| $\Phi_{ij}$ | pair potential interaction between *i* & *j* |

## 1. INTRODUCTION

Advances in electronic miniaturization and nanodevices are solving complex problems across many industries, from space exploration to medical advances. As micro-nano electronics are being developed at smaller scales, the topic of heat transfer becomes an important design feature in their performance. Smaller, lighter integrated circuits can optimize form factor, however as they decrease in size, their performance becomes more influenced by the small-scale phenomena at the interface of materials. Heat dissipation capacity can determine the performance and total life cycle of such devices. Therefore, working towards a fundamental understanding of nanoscale heat transfer phenomena is of

upmost important for the continued success of miniaturization of electronic devices.

Thermal management has been widely investigated in the microscale for cooling devices [1-8]. Earlier studies have suggested heat transfer enhancement of nanofluid through several methods stating the addition of nanoparticles can affect convective heat transfer more than base fluid flow, especially when the size and shape are varied [9-11]. Although experimental and theoretical methods have been widely studied, experiments continue to be costly and difficult to carry out. Incorporating suspended solid nanoparticles, i.e., nanofluids, via molecular dynamics has been an increasing interest to researchers recently to study the effect of fluid flow and its thermal properties. Studies have been done to observe enhancement of heat transfer through changing surface geometry and topography of nanochannels. Jiang et al. and Bantan et al. used a zig zag nanochannel to show thermal behavior of copper nanoparticles in water as the base fluid. [12,13] It was found that adding nanoparticles can show a promising parameter for increasing heat transfer, utilizing the Green-Kubo method for thermal conductivity. Kalteh et al. investigated the convective heat transfer of argon in a simulated rough nanochannel presenting results of an increase of Nusselt number when increasing the nanochannel size [14]. The roughness of the nanochannel, specifically also increases the Nusselt number as well as the velocity of the base fluid. D. Wen et al. conducted experimental investigations of laminar flow of nanofluids to study the convective heat transfer [15]. They report that $Al_2O_3$ nanoparticles dispersed in de-ionized water increased convective heat transfer particularly at the entrance region due to a decrease along the nanochannel. Alipour et al. further investigated other wall material by observing copper and platinum square nanochannels with different geometric roughness at the inner surface [16]. Results showed that the average velocity and temperature of particles are greater with cuboid and hemispheroid roughness by applying a constant driving force. Several researchers also performed experiments to quantify convective heat transfer to show how wall surface conditions can enhance heat transfer in microchannels [17-20]. Their study showed that Nusselt number was higher for a rough wall compared to smooth walls. Additionally, Noorian et al. utilized molecular dynamics to simulate rough walls through various checker surface roughness [21]. In this paper, the attraction energy of fluid-solid interaction was investigated which further showed how introducing rough walls enhances the effects on flow velocity even with more particles trapped between extruded segments. Song et al. was able to compare base fluid flow with sinusoidal wall structures enhancing heat transfer for better heat dissipation [22]

As can be seen in previous work, most molecular dynamic simulations for heat transfer studies of nanochannels have been studied with various surface roughness and geometry. Although this area of work does show heat transfer enhancement, aggregating nanoparticles to study the effects are not as extensive but have been noted to enhance heat transfer.

In this paper, we investigate the thermal behavior of fluid with a single nanoparticle of various diameters. An investigation of how one nanoparticle can affect the system has not been conducted in this manner which would provide an insight into fundamental understandings of nanochannel flow. MD simulation method is utilized to conduct all variations of this study to investigate the convective heat transfer and velocity effect. By calculating the Nusselt number, we can quantify the thermal enhancement of different size nanoparticles.

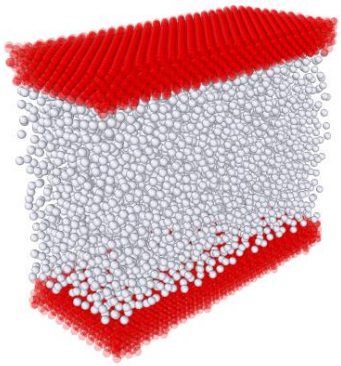

**FIGURE 1:** SIMULATION MODEL SET OF COPPER ATOMS (RED) AND ARGON FLUID ATOMS (WHITE) PROVIDED BY OVITO VISUALIZATION TOOL.

## 1. MATERIALS AND METHODS

### 2.1 Model and simulation method

A Poiseuille flow was observed in a nanochannel between two parallel fixed walls comprising of a single nanoparticle embedded into the base fluid. All molecular dynamics simulations were carried out through LAMMPS software and OVITO was used as the visualization tool for capturing snapshots of the model. [23,24]. Figure 1 shows the 3D snapshot of the nanochannel model. Figure 2 shows the setup and initial position of the nanoparticles embedded in the fluid. Argon atoms were selected as the fluid due to its simplicity of modeling allowing for a close focus on phenomena of heat transfer and fluid flow characteristics without the need of complexities associated with other fluids. For this reason, it is a common material when studying systems in molecular dynamics. Copper was selected as the solid upper and lower wall as well as the aggregated nanoparticle.

**TABLE 1:** This table provides the parameters to estimate the LJ two body interactions between argon atoms and copper/argon atoms.

| LJ Parameters | Ar-Ar | Cu-Ar |
|---|---|---|
| σ(Å) | 3.405 | 2.871 |
| ε(J) | $1.67 \times 10^{-21}$ | $10.4153 \times 10^{-21}$ |

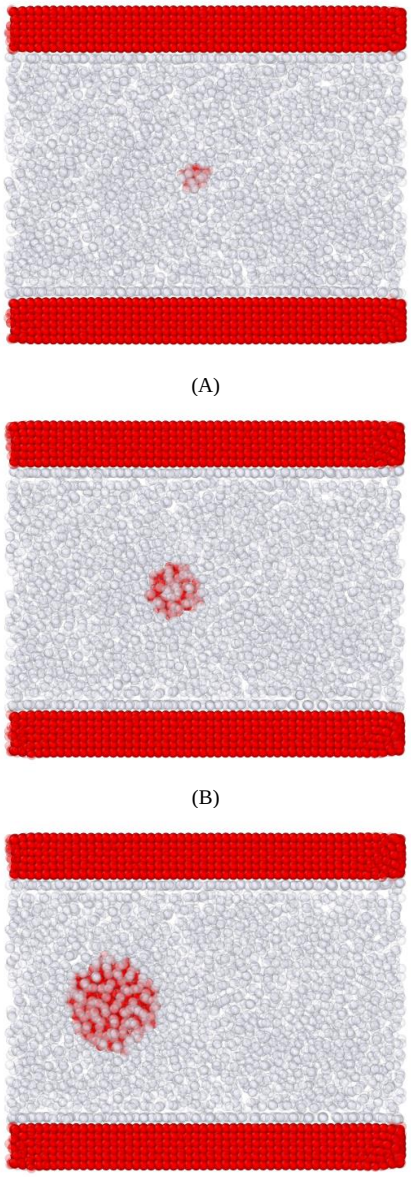

(A)

(B)

(C)

**FIGURE 2:** 3D RENDERING OF DIFFERENT DIAMETER SIZES IN THE NANOCHANNEL FOR (A) 0.8 NM (B) 1.25 NM (C) 2 NM.

The simulation box is defined by 95 x 40 x 80 Å$^3$ ($x$ x $y$ x $z$). Each wall has a thickness of 10 Å resulting in a constant channel height of 60 Å. To properly apply a thermostat to the fixed wall, an inner and outer layer is modeled for each wall. The outer layer of each wall will represent the adiabatic condition in which the atoms are frozen to their initial coordinates (velocity is zero) to prevent any deformation. "Phantom atoms" make up the inner layer which acts as the heat source of the system through a given thermostat. Additionally, the inner solid wall atoms are constrained via harmonic springs with a spring constant of 70 N/m [25]. Periodic boundary conditions are applied in x, y, and z directions. However, a quasi-boundary condition will be modeled in the x-direction of fluid flowing by placing a force region and thermostat region at the simulation box inlet [26]. At the nanochannel outlet Argon atoms will enter the force region and will accelerate with a constant force. Upon entering, their temperature is reset at the desired inlet temperature to observe convective heat transfer between the cold walls and hot liquid. Argon atoms are arranged by face-centered cubic (FCC) lattice structure and confined in the channel with number of atoms at a density of 1200 kg/m$^3$ corresponding with the different volumes of the nanoparticles and with a lattice constant of 4 Å [25]. The copper wall and nanoparticles are also created by FCC lattice structure with a lattice constant of 3.61Å.

The interatomic interactions between the solid wall and fluid to describe Ar and Cu can be modeled after the well-known 12-6 Lennard-Jones (LJ) potential given by equation (1):

$$\Phi_{Lj}(r) = 4\varepsilon\left[\left(\frac{\sigma}{r_{ij}}\right)^{12} - \left(\frac{\sigma}{r_{ij}}\right)^{6}\right] \quad (1)$$

where σ and ε are the distance between two interacting particles at zero energy and the well depth (dispersion energy) that describes the magnitude of attraction or repulsion, respectively. The parameter for Ar-Ar and Cu-Ar are ε(Ar) = 1.67 x 10$^{-21}$ J, σ(Ar) = 3.405 Å, ε(Cu) = 65.625 x 10$^{-21}$ J, σ(Cu) = 2.337 Å [27]. The LJ potential parameters for Cu-Ar, the Lorenz-Bertholot mixing rule can be applied by [28]:

$$\varepsilon_{sl} = \sqrt{\varepsilon_s \varepsilon_l} \quad (2)$$

$$\sigma_{sl} = \frac{\sigma_s + \sigma_l}{2} \quad (3)$$

Where $s$ denotes the solid parameter and $l$ is the liquid parameter. Therefore, from both equations (2) and (3), σ and ε for Ar-Cu are 10.4153 x 10$^{-21}$ J and 2.871 Å, respectively.

To obtain a more precise model for interatomic interactions between copper atoms, the embedded atom method (EAM) potential [29,30] is adopted and shown in equation (4)

$$U = \sum_i F_i\left(\sum_{j\neq i}\rho_i(r_{ij})\right) + \frac{1}{2}\sum_{j\neq i}\Phi_{ij}(r_{ij}) \quad (4)$$

where $Fi$ is the embedding energy which is a function of the atomic electron density $p$, $\Phi$ is the pairwise potential interaction, and alpha and beta represent element types of atoms $i$ and $j$, respectively. The cut-off radius for both L-J and EAM potentials are set to $R_{cut}$ = 10 Å. This will ignore atomic interactions beyond the distance as energy is not substantial enough to affect the system at those distances.

Utilizing the *hybrid* method, both potential models were combined to interact alongside their determined constants. These potential parameters were defined using the *pair_coeff* command in conjunction with the Cu_u3.eam file for copper atoms. For a binary potential system selected in this study , interaction force between atomic pairs can be derived from the potential model as such to form a relation as shown in equation (5).

$$\vec{F_i} = \sum_{i \neq j} F_{ij} + \overrightarrow{F_{ext}}$$
$$\overrightarrow{F_{ij}} = -\vec{\nabla}(\Phi + \Phi_w) \quad (5)$$

where $F_{ext}$ is the external driving force per molecule at the inlet in the x direction (forced flow). By integrating equation (5), the position ($r_i$) and velocity vector ($v_i$) can be found and a calculation using $r_i$ and $v_i$ could obtain thermodynamic properties of the simulation domain [21]. Initial velocities are defined by a *compute* command for the flow of fluid using a temp/profile function. This will calculate the temperature bias needed to remove the mean flow velocity that contributes to the overall temperature, defined as the thermal velocity. Therefore, fluid flowing in the nanochannel can be calculated by equation (6):

$$T = \frac{1}{3Nk_b} \sum_{j=1}^{N} m_j \left(v_j - v_{ave}\right)^2 \quad (6)$$

Where T is the temperature, $k_b$ is Boltzmann constant, N is the number of atoms, $m_j$ is the atom mass of atom j, $v_j$ is the velocity of atom j and finally, $v_{ave}$ is the mean flow velocity of the defined bin. The atomic masses of Cu and Ar were assumed to be 63.546 g/mol and 39.948 g/mol.

### 2.2 Equilibrium and flow conditions creation

In the simulation domain, all atoms are created by FCC lattice, therefore in order to reach equilibrium and subsequently a steady state, the system must be relaxed [31]. Molecular dynamics simulation begins by organizing both Ar and Cu atoms in their respective region with a particular coordinate and initial velocity. A minimization technique is applied to the system to ensure particles begin at their local potential energy minimum. All simulations are performed with the velocity Verlet algorithm to calculate the trajectories of the particles through integration of Newton's equations of motion at each timestep. A recommended time step of 1 fs is selected, and the system can be relaxed in a Nose Hoover heat bath at 200 K at the walls in conjunction with an NVE ensemble for the fluid. Both perform time integration which update the position and velocity for atoms in the group for each timestep, however NVT performs both time integration and thermostatting, therefore it is imperative to select the proper ensemble for individual groups (e.g., walls and fluid). To determine when the system reaches equilibrium, potential and total energy is observed over time. A total of 1ns (1 x $10^6$ time steps) is determined to sufficiently stabilize the system reaching an equilibrium state. Once the system is relaxed, flow conditions can then be applied to the nanochannel for a total of 4ns (4 x $10^6$ time steps) which will be used for sampling. Before the nanochannel inlet, two regions are considered (force region and thermostat region) to set up the quasi-periodic boundary condition for the system. The initial region is the force region with a length of 10 Å in the x-direction and is located at -15 Å < x < -5 Å. In this dynamic region, a force of 0.002 eV is applied to create flow movement. Following right after is the thermostat region with a length of 5 Å in the x-direction and is located at -5 Å < x < 0 Å. In this dynamic region, the temperature of each atom that flow in this space will enter a Nose-Hoover thermostat bath set at 300 K which resets their temperature before entering the nanochannel.

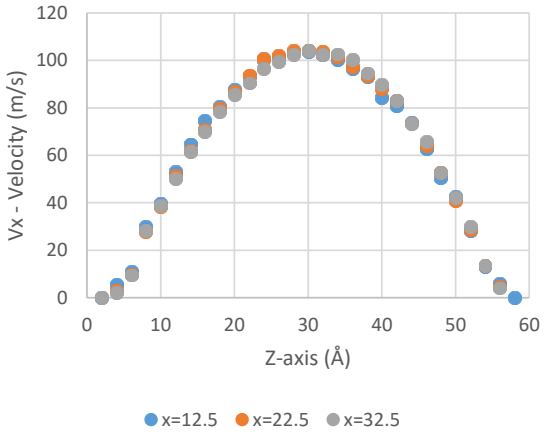


**FIGURE 3:** VELOCITY PROFILE OF A .8NM NANOPARTICLE ALONG THE X-DIRECTION AT THREE DIFFERENT POINTS.

## 3. RESULTS AND DISCUSSION

It should be noted that the geometry of the system was also optimized to prevent any defects introduced by LAMMPS along with minimizing the error of the thermodynamic results with respect to published results. After steady state conditions is reached, data is obtained from the *fix ave/chunk.*

To calculate the velocity and obtain the temperature values, the sampling region is partitioned into 2D pencils divided by a total of 817 bins in the x and z direction of the nanochannel. The size of each bin is 5 x 2 x40 $Å^3$. In order to observe the behavior of nanofluid flow, the velocity is calculated for each diameter size as shown in Table 1. Based on Figure 3, we see that the velocity for on single nanoparticle is the same through the nanochannel. Steady state conditions provided for a collective

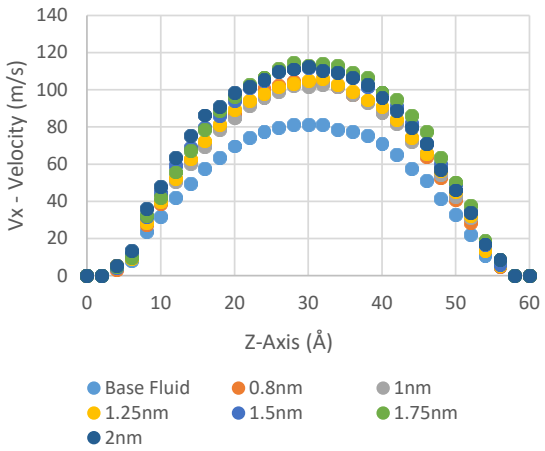


**FIGURE 4:** VELOCITY PROFILE ACROSS THE NANOCHANNEL AT X = 22.5 Å FOR BASE FLUID AND ALL NANOPARTICLE DIAMETER SIZES.

flow across the nanochannel. Base liquid flow is also simulated as a benchmark to observe how velocity and temperature is affected by adding different size nanoparticles. Figure 4 shows the velocity profile of various cases at 22.5 Å. The velocity profile obtained directly from MD simulation demonstrates the hydrodynamically developed laminar flow [33,34]. Moreover, it is important to note that by observation, there is no velocity slip at the walls for all cases. This may be due to the energy parameter calculated from the Lorenz -Bertholot mixing rule [ 34] Additionally, it was also observed that argon fluid flowing in a copper walled nanochannel were reported to have little to no velocity slip than other materials such as Platinum [ 35]. Based on the figures provided we can conclude that the nanoparticles are traveling at high velocities . By introducing a single nanoparticle, the fluid flow rate increases when compared to base fluid reaching a magnitude of 114 m/s. This trend agrees with previous work that demonstrates a higher velocity profile of nanofluid than base fluids of the same conditions [ 13, 26,27,36, 37]. It is important to note that there is no trend regarding the size of the nanoparticle. Increasing the diameter of the single nanoparticle does not necessarily increase the flow rate of the fluid which is reaffirmed in Bao & Zhong et al [3 8]. This is in part due to the surface to volume ratio of nanoparticles with respect to the nanochannel. This study showed that an excessive number of nanoparticles can increase the viscosity of the nanofluid resulting in a decrease of velocity overall. Even with a single nanoparticle, we see this behavior in which although an increase is observed, there is no direct trend based on the size, rather it is dependent on the volume concentration of the nanofluids. In the figure, we see that for diameter size 0.8 nm , 1 nm, and 1.25 nm, the velocity in the middle is roughly 104 m/s. For diameter sizes 1.5 nm, 1.75 nm, and 2 nm, we see the average velocity in the middle around 114 m/s while the base fluid reaches only 81 m/s.

Temperature profiles were obtained from the simulation after reaching steady state and shown to vary across the different diameter sizes. The temperature profile of base fluid is shown in Figure 5. Here, the middle of the region has a maximum temperature of 215 K after reaching a steady flow with n o nanoparticles. Also, from previous studies, we see the heat dissipation along the nanochannel which was expected. It was also expected to show higher temperatures at both the walls and in the middle of the fluid, however based on these results directl from MD simulations, the temperature at the of the argon layer at the walls are lower and the overall temperature of the fluid is

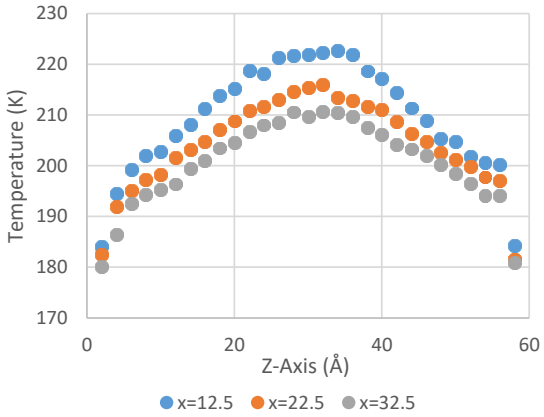


**FIGURE 5:** TEMPERATURE PROFILE OBTAINED FROM MD SIMULATIONS OF BASE FLUID SHOWING TEMPERATURE JUMPS AT THE WALL.

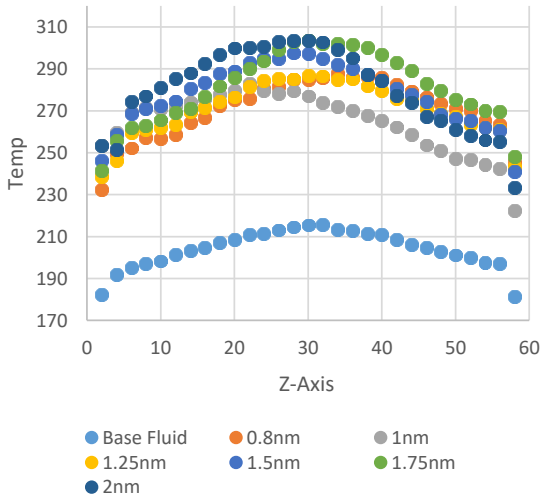


**FIGURE 6:** TEMPERATURE PROFILE OBTAINED FROM MD SIMULATIONS OF BASE FLUID AS WELL AS ALL DIAMETER SIZES OF NANOPARTICLES SHOWING VERY LARGE AVERAG TEMPERATURE GAP BETWEEN THEM.

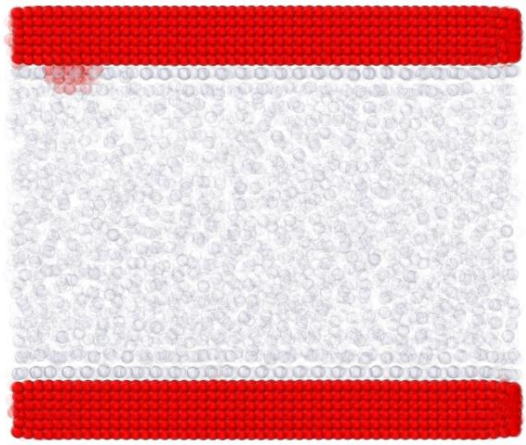

**FIGURE 7:** SNAPSHOT OF THE 1 NM NANOPARTICLE ADHERING AND LINGERING AT THE WALL DUE TO STRONG INTERACTIONS.

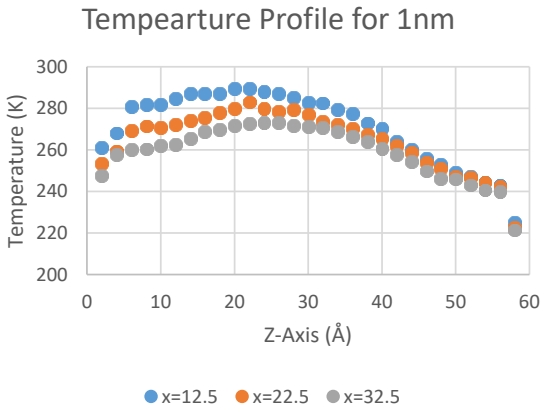


**FIGURE 8:** TEMPERATURE PROFILE OF 1 NM SIZE NANOPARTICLE AT DIFFERENT POINTS ACROSS THE NANOCHANNEL.

greatly reduced which makes for an interesting observation. This can be due to incorrect velocity bias removal of the mean flow velocity of each bin. In Figure 6, the temperature profiles are plotted along the nanochannel for different cases. At this point it is important to note an unrealistic axial heat conditions oc curs from the hot images of the outlet atoms to the inlet atoms of the nanochannel resulting in temperature differences. Therefore, in order to showcase the most accurate results, data is only gathered from the first half of the nanochannel. It is evident that in this simulation model, the nanoparticles produce a higher temperature profile that that of the base fluid. This contradicts the results of several papers with the aggregation of nanoparticles result in lower temperatures across the nanochannel. However, Toghraie et al. showed that when adding more nanoparticles inside the surrounding fluid of the nanochannel, the temperature does tend to increase [21]. Moreover, we see that the temperature increases overall as the diameter of the nanoparticle size increases. The results also show that the temperature at the wall of the base liquid is lower than the nanofluid which is consistent with previous work regarding the solid-like layer present close to the upper and lower walls. In all simulations this solid-like layer is present but more prominent for base fluid as there are more argon atoms that can accumulate and form this phenomenon at the wall. Moreover, the temperature distributions and maximum values tend to vary across the cases. This can be due to the nanoparticle's chaotic translational movement across the nanochannel. This is evident in the case of the 1 nm particle size shown in Figure 7 where the nanoparticle tends to attach itself close to the wall . We see the distribution skewed closer to the left as shown in Figure 8 which is due to the strong attraction force between copper atoms from EAM model. It is evident that there is more heat transfer at the upper wall where the nanoparticle is located as the overall temperature is lower at that location looking at the figure. Several researchers have used identical models in their nanofluids flow in MD, so perhaps the size of the nanochannel in conjunction with the chaotic movement leads the particle to attach itself to the walls. It was also observed that the attachment can occur at the upper or lower wall. One solution is to run the simulation at a larger force to see if applied momentum is able to streamline the particle so that it does not have a chance of adhering. This seems to occur more so to the s maller diameter sized nanoparticles (i.e., 0.8 nm. 1 nm, and 1.25 nm) . Although not clear, a larger force may be needed to ensure the nanoparticl is driven across the nanochannel without adhering to the walls.

To investigate the heat transfer of all the given situations, a dimensionless parameter is calculated to quantify how convective heat transfer changes. By calculating the bulk temperature given by equation (7):

$$T_b = \frac{\int_0^L \rho(z) V_x(z) T(z) dz}{\int_0^L \rho(z) V_x(z) dz} \quad (7)$$

where ρ is the fluid density $V_x$ is the velocity in the x -direction both averaged within each bin across the nanochannel height. The Nusselt number can then be defined by equation (8)

$$Nu = \frac{L}{T_b - T_w} \frac{\partial T}{\partial z}\Big|_{z=0} \quad (8)$$

where Tw is the wall temperature, L is the nanochannel height, and $T_b$ is the bulk fluid temperature calculated previously.

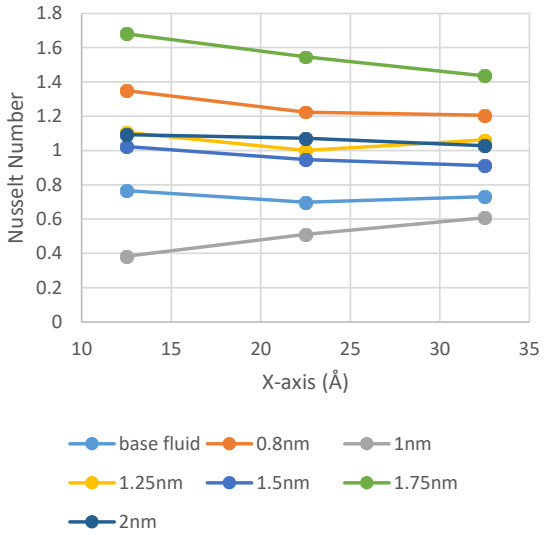


**FIGURE 9:** NUSSELT NUMBER OBTAINED FROM MD SIMULATIONS OF ALL NANOPARTICLE DIAMETER SIZES.

Taking a closer look at a single diameter nanoparticle in Figure X, we see that th e Nusselt number decreases along the nanochannel as expected from previous studies. While the temperature increases as the diameter size increases, the Nusselt number shows a relative similar pattern. However, the Nusselt number actually increases for the different cases as seen in Figure X. Here we see that increasing the diameter size does not necessarily mean that the Nusselt number is increased. Diameter size 1.7 nm seems to have a higher Nusselt number than the other cases. However, the nanoparticle of 1 nm seems to produce the lowest Nusselt number which increases across the nanochannel. This may be due to the nanoparticle adhered to the solid -liquid interface for an extended period of time.

## 4. CONCLUSION

In this study, a nanochannel with parallel copper walls and argon fluid atoms with flow conditions are investigated. Its aim is to observe behavior and convective heat transfer of nanofluid with a single spherical copper nanoparticle . Simulations were carried out by LAMMPS code, and all data is collected from their results. Velocity profiles show that adding a nanoparticle can increase the velocity, however, increasing the nanoparticle diameter does not necessarily mean the velocity increases. To examine th e heat transfer, temperature profiles were observed. They show that adding a single nanoparticle increases the temperature of the fluid closer to the inlet resulting in a lower heat transfer characteristic. The Nusselt number is also investigated to quanti fy the heat transfer characteristic of the system in comparison to base liquid. Results show that with an increase of diameter size of the nanoparticle, the Nusselt number can vary but typically increases which is due to the high temperature jump at the wa ll to the solid-like later of the fluid.

## ACKNOWLEDGEMENTS

This paper would not have been possible without the continued support and positive encouragement from Dr. Deify Law.

## REFERENCES

[1] R. Kamali, S. Movahed, *ASME Proceedings Paper*, 2009, 1425-1430

[2] D. B. Tuckerman and R. F. W. Pease, *IEEE Electron Device Letters*, vol. 2, no. 5, pp. 126-129, May 1981

[3] S. Poudel, A. Zou, S. C. Maroo, 2021

[4] C. Wang, Y. Kazoe, K. Morikawa, H. Shimizu, Y. Pihos K. Mawatari, T. Kitamori, *The Royal Society of Chemistry*, 2017, 7, 50591-50597

[5] Sarit K Das, Nandy Putra, Wilfried Roetzel, *International Journal of Heat and Mass Transfer* , Volume 46, Issue 5, 2003.

[6] C.W. Sohn, M.M. Chen, *J. Heat Transfer, Trans. ASME* 103 (1981) 47–51.

[7] A.S. Ahuja, J. Appl. Phys. 46 (1975) 3408–3416.

[8] A.S. Ahuja, J. Appl. Phys. 46 (1975) 3417–3425.

[9] Putra, N., Roetzel, W. & Das, S.K. Natural convection o nano-fluids. *Heat and Mass Transfer* **39,** 775–784 (2003).

[10] D. Wen, Y. Ding, *International Journal of Heat and Mass Transfer*, Volume 47, Issue 24, 2004, Pages 5181 -5188, ISSN 0017-9310

[11] Lee, S., Choi, S. U., Li, S., and Eastman, J. A., *ASME. J. Heat Transfer.* May 1999; 121(2): 280–289.

[12] Y. Jiang, S. Dehghan, A. Karimipour, D. Toghraie, Z. Li, I. Tlili, *International Communications in Heat and Mass Transfer*, 2020, 116, 104652.

[13] R. A. R. Bantan, N. H. Abu-Hamdeh, O. K. Nusier, A. Karimipour, *Journal of Molecular Liquids*, 2021,331,115714.

[14] M. B. Motlagh, M. Kalteh, *International Journal of Thermal Sciences*, 2020, 156, 106472.

[15] D. Wen, Y. Ding, *International Journal of Heat Mass transfer*. 47 (2004) 5181-5188.

[16] P. Alipour, D. Toghraie, A. Karimipour, M. Hajian, *Journal of Molecular Liquids*, 2019, 275, 192-203.

[17] M. Wang, H. Sun, L. Cheng, *Journal of Molecular Liquids*, 2021, 341, 116908.

[18] S. Ghahremanian, A. Abbassi, Z. Mansoori, D. Toghraie, *Chinese Journal of Chemical Engineering*, 2021, 27.

[19] R. Kamali, A. Kharazmi, *International Journal of Thermal Sciences*, 2011, 50, 226-232.

[20] C. Zhang, Y. Chen, M. Shi, *Chemical Engineering and Processsing: Process Instensification*, 2010, 49, 118-1192.

[21] H. Noorian, D. Toghraie, A. R. Azimian, *Heat and Mass Transfer*, 2014, 50, 105-113.

[22] Z. Song, Z. Cui, Q. Cao, Y. Liu, J. Li, *Journal of Molecular Liquids*, 2021, 337, 116052.

[23] S. Plimpton, J. Comput. Phys. 117, 1 (1995).

[24] A. Stukowski, Modelling Simul. Mater. Sci. Eng. 18, 015012 (2010).

[25] S. Ge, Y. Gue, M. Chen, *Molecular Phys.* 113, 7, (2015).
[26] M. B. Motlagh, M. Kalteh, *Journal of Molecular Liquids*, 2020, 318, 114028.
[27] M. B. Motlagh, M. Kalteh, *Journal of Molecular Liquids*, 2020, 111, 104478.
[28] L. Li, Y. Zhang, H. Ma, M. Yang, *Journal of Nanoparticle Research*, 12, 811-821 (2010).
[29] S. M. Foiles, M. I. Baskes, M. S. Daw, *Phys. Review B*, 1986, 33, 12.
[30] W. Cui, Z. Shen, J. Yang, S. Wu,*Case Studies in Thermal Engineering*, 6, 182-193, (2015).
[31] C. Hu, M. Bai, J. Lv, P. Wang, L. Zhang, X. Li, *Microfluidics and Nanofluidics*, 2014, 17, 581-589.
[32] D. C. Marable, S. Shin, A. Y. Nobakht,*International Journal of Heat and Mass Transfer,*2017, 109, 28-39.
[33] J. Lahjomri, A. Oubarra, *Journal of Heat Transfer*, 1999, 121, 1078-1083.
[34] Q Sun, K. Choi, X. Mao, *International Journal of Thermal Sciences*, 2021.
[35] A. Asgari, Q. Nguyen, A Karimipour, Q. Bach, M. Hekmatifar, R. Sabetvand, *Journal of Molecular Liquids,* 2020, 318, 114023.
[36] A. Arjmandfard, D. Toghraie, B. Mehmandoust, M. Hashemian, A. Karimipour, *Int. Comm. In Heat and Mass Transfer,*2020. 118, 104874.
[37] D. Toghraie, M. Mokhtari, M. Afrand, *Physica E,* 2016, 84, 152-161.
[38] Bao L, Zhong C, Jie P, Hou Y.*Advances in Mechanical Engineering*. 2019, 11, 1-17.

**Fresno State Indoor Air Quality Research Project Report**
**Research Project Report Title:** A Mitigation Study of Air Treatment Technology with a Physical Air Filter on Volatile Organic Compounds, Carbon Dioxide, and Fine Particulate Matters Generated by Indoor Smoke

**Authors:** Deify Law and Vincent Malpaya
**Authors' Affiliation:** California State University, Fresno

**Date:** February 5, 2022

**Submit to:** ASHRAE San Joaquin

**Keywords:** Bipolar ionization, volatile organic compounds, particulate matters, smoke, indoor environment

## 1. Introduction

The recent SARS-CoV-2 outbreak has shed new light and renewed interest on the need for maintaining good indoor air quality (IAQ). In doing so, technologies invented over the past ten years have garnered interest to combat the virus. One such technology is Bipolar Ionization (BPI). BPI manufacturers have claims of reducing or eliminating odors, volatile organic compounds (VOC), killing viruses or bacteria, and reducing airborne particles that cannot be commonly or easily filtered. Manufacturers have conducted individual tests in controlled labs to show results and effectiveness of the air treatment technology. However, third party independent testing is largely absent [1].

California Energy Commission (CEC) has a fundamental energy goal of being Zero Net Energy (ZNE) by 2020 for new residences, and 2030 for all new commercial buildings. The common solution includes offsetting energy usage with solar; yet, innovation to actively reduce energy demand without sacrificing comfort or safety is paramount. The Central Valley presents one of the biggest obstacles in achieving the stated goals from an HVAC perspective. The most populous areas of the state can maximize outside air (OSA) to offset mechanical cooling or heating with favorable climates and reduced pollutants. The Central Valley cannot easily make this conversion because of its extreme heat and varying air pollution, caused by smog, smoke, and airborne pollutants from wildfires, transportation, large industries, and local farming. As such, any additional OSA entering the building must be conditioned and filtered. However, if BPI technology can prove to be effective at filtering and purifying the return air to a point where OSA can be reduced or eliminated (as some manufacturers claim), then a reduction of the power consumption can be realized [1].

All the aforementioned goals or issues prompted a collaboration between Fresno State and American Society of Heating, Refrigerating, and Air-Conditioning Engineers (ASHRAE) San Joaquin Chapter to identify the best air treatment and filtration strategy to mitigate the VOCs and fine particulate matters (PM) concentrations caused by, in particular, a smoke contaminant source. ASHRAE San Joaquin Chapter reached out to Dr. Deify Law in the Spring 2021 semester, an associate professor in the Department of Mechanical Engineering from the Lyles College of Engineering at Fresno State, to test numerous combinations of filter (minimum efficiency reporting value or MERV and high efficiency particulate air filter or HEPA) and air treatment technology (BPI and UVC light) for assessing IAQ given an indoor space contaminated by a woodchip-based smoke source. Woodchip-based smoke is made up of very small particles, gases, and water vapor. Gases include carbon dioxide, carbon monoxide, nitrogen oxide, and volatile organic compounds. The primary goal of the research project is to evaluate the impact of using the BPI, if any, on mitigating the VOC, $CO_2$, and PM concentrations caused by the smoke contaminants. BPI is commonly reported to (i) reduce airborne particulate matters by causing them to cluster or agglomerate and form larger particles that can settle out of the air more rapidly or be filtered more effectively, (ii) neutralize odors and break down volatile organic compounds (VOCs), (iii) inactivate or kill viruses and other microorganisms, and (iv) reduce the amount of required outdoor air [2]. Many engineers have been recommending BPI because of it's relatively low upfront cost, low maintenance and materials costs, and the low static pressure drop to air handling units. One area to note is the possibility of ozone generation from these devices. Many

manufacturers of these devices have certified their products to UL standards 867, 867A and UL 2998, Verified Ozone Free. However, there is a significant lack of published literature to document the filtration and air treatment effectiveness of bipolar ionization devices.

Bipolar ionization devices come in 2 different varieties, each using a different mode of operation. Needlepoint bipolar ionization (NBI) is where the ions are emitted into the airflow by needles or carbon brushes or other needlepoint type emitters. Dielectric Barrier Discharge bipolar ionization (DBD) uses a sealed cathode tube to create a plasma discharge which will emit ions into the airflow. Of the 2, DBD bipolar ionization has a longer history of application, study and usage, with literature dating back to the 1970's.

In the Spring 2021 semester, Dr. Deify Law, an associate professor from mechanical engineering department at Fresno State, identified a stand-alone fire prop house chamber at the Fire Academy site of the Fresno City College (FCC) Career and Technology Center (CTC) to meet the objective of the IAQ research project. The house chamber is 400 $ft^2$ and 8 ft high and it has a garage space to store the IAQ research equipment unit. The IAQ research equipment unit comes with a Carrier Opticlean negative air machine unit, Trane 3-ton packaged rooftop air-conditioning unit, and rigid and flexible ducts. Filter and air treatment technology devices were mounted inside the units and ducts. IAQ BELIMO sensors and TEMTOP fine particulate matter (PM) handheld monitors were mounted at the return and supply air locations of the airflow duct passage. VOC, carbon dioxide ($CO_2$), and PM concentrations were measured from each respective sensor/monitor location. There are two manufacturers of BPI technology, DBD and NBI devices, and they were all mounted inside the air duct at the supply air duct location.

The project objective is to perform the IAQ tests over a two-phase research cycle. The present phase of work is to evaluate IAQ with different air treatment technologies in conjunction with physical air filters. Per the contractual agreement between Fresno State and ASHRAE San Joaquin Chapter, outside air opening must be sealed closed, only one fan can be used, and the cooling coil must not be used in this phase of research. UVC lights are tested to test industry claims instead of industry norms in this present work. Depending on the test results from the present phase of work, the second phase of work will be proposed. The research team includes student Mr. Vincent Malpaya and faculty Dr. Deify Law who performed the IAQ research experiments.

The filtration system combinations consist of MERV 8, MERV 13, and HEPA physical filters and each physical filter is combined with either NBI manufacturer device, or DBD manufacturer device, UVC lamp, or not combined with any air treatment technology device. Every air treatment technology device will be combined with every physical filter one at a time for testing. Each filtration system combination test recirculated the air for 30 minutes after the smoke saturated the indoor space. VOC and $CO_2$ concentration reductions over the sensor/monitor locations as well as PM removal efficiency will be determined quantitatively or qualitatively based on the measurements.

## 2. **Methods**

Figure 1 demonstrates the set-up of the present air filtration and treatment test in a schematic. The components of the test setup include both supply and return air flexible ducts and two TEMTOP air quality handheld monitors, smoke hose and smoke outlet, Johnson Controls zone sensor, four BELIMO indoor air quality sensors, physical filters, air treatment technologies, Carrier Opticlean negative air machine, and Trane packaged rooftop air-conditioning units (relevant figures are included in the appendix). The test set up occupies both the L-shaped indoor and garage spaces of the fire prop house as indicated in the Figure 1 (a) physical schematic and (b) flow diagram of a test set up. There was one small room of the house that was fully enclosed, and it was not part of the test study. The Johnson Controls zone sensor measured indoor zone temperature and $CO_2$ concentration whereas each BELIMO sensor installed by the Johnson Controls Company measured VOC concentrations in percentages and $CO_2$ concentrations in parts per million (ppm). The airflow was maintained with 100% return air by closing the economizer using a duct-taped cardboard. Figures 1 (c) shows a general timeline of a test condition. Each air filtration system combination test lasted for about an hour. Smoke was not introduced to the L-shaped indoor space (indoor space) and only baseline temperature, PM concentrations, $CO_2$ concentrations, and VOC percentages were measured in the first 10 minutes of the 1-hour test duration. Then, woodchip-based smoke was introduced to the indoor space and it lasted for 5 minutes. Next, the fan of the Carrier Opticlean negative air machine was turned on at its highest fan mode for 30 minutes, which its purpose was to return the contaminated air for filtration and air treatment. The air treatment device if needed will also be active for 30 minutes. Finally, both the fan and air treatment device will be switched off and the tested indoor environment will be left for settling down during the last 15 minutes of the test duration. All sensors and monitors' data were logged over a one-minute time resolution during the 1-hour test duration. Figure 1 (d) shows the offset view of supply and return air ductworks to complement the information presented in Figure 1 (a).

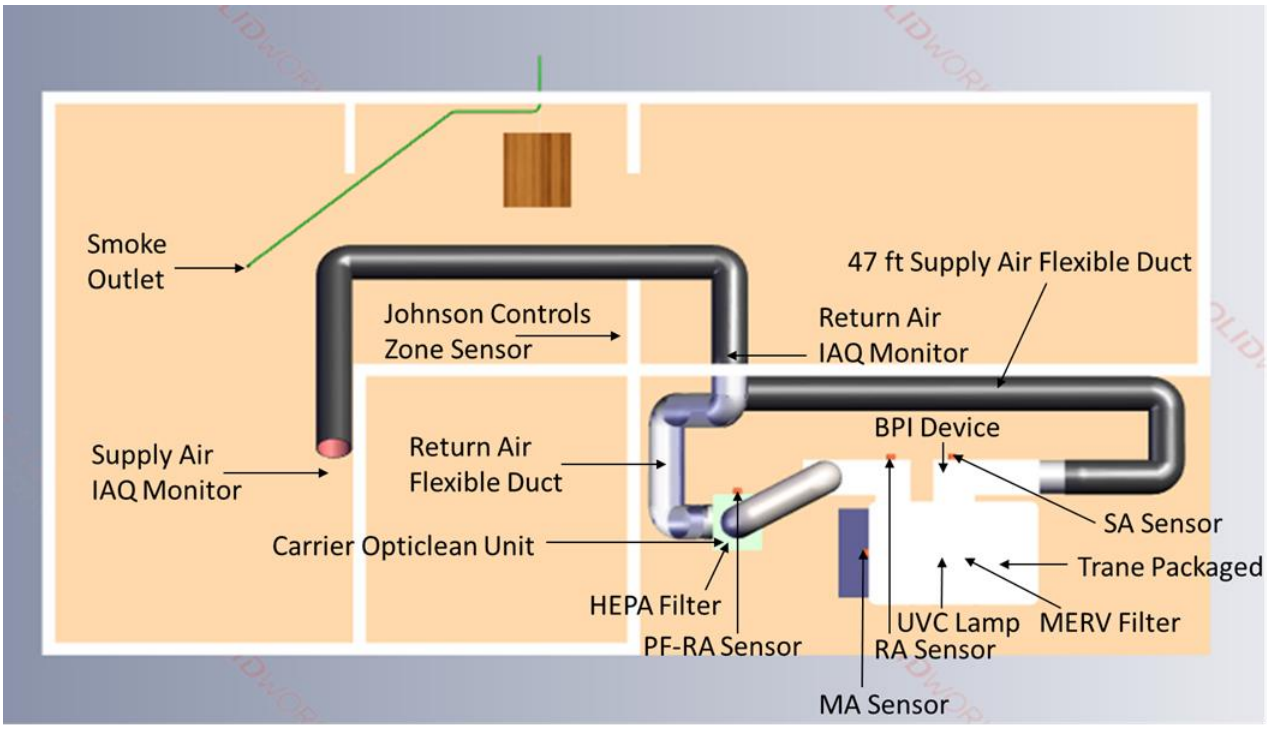


(a) Physical schematic of a test setup

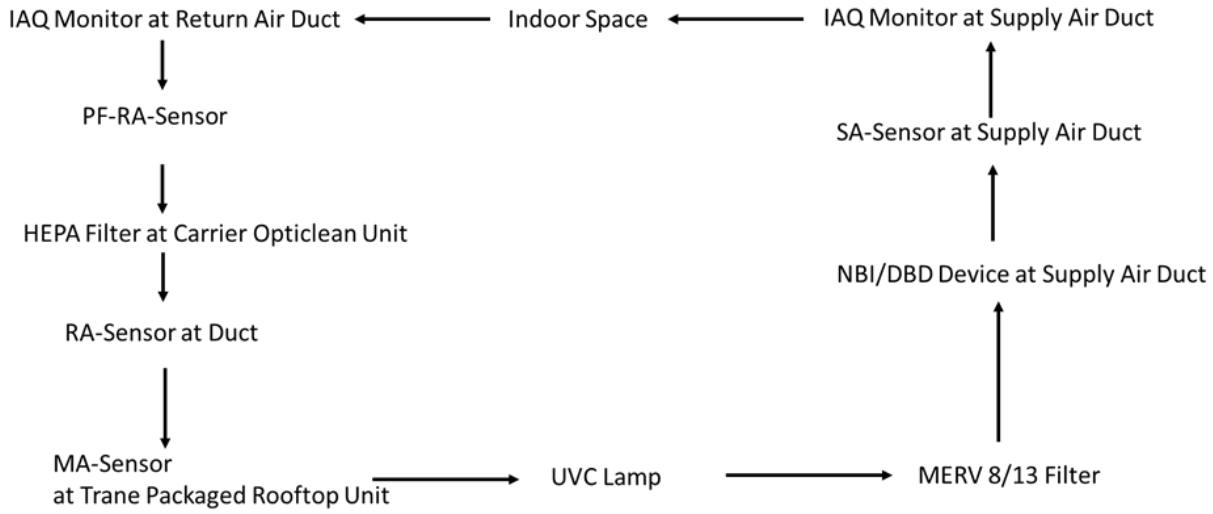


(b) Flow diagram of a test set up (Note: this diagram is meant to show the location of filter, air treatment technology, and sensor in the test set up. Filter and air treatment technology will only be included if they are part of the particular test condition.)

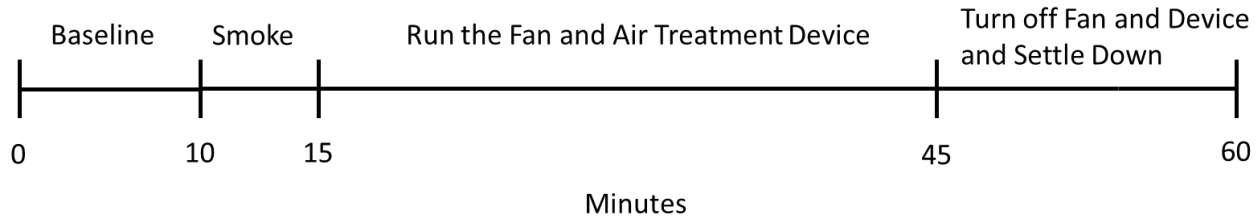

(c) General timeline of a test condition

(d) Offset view of supply (bottom black) and return (top transparent) air ductwork

Figure 1. (a) Physical schematic, (b) flow diagram, and (c) general timeline of a test condition, and (d) offset view of supply (bottom black) and return (top transparent) air ductwork.

## 3. Results and Discussion

### 3.1 Airspeed, Ambient Temperature, and Relative Humidity

A hot-wire anemometer was used to measure the airspeeds at the supply and return air ducts and the measurement was approximately 1250 ft/min through a 14 inches diameter air duct in all test conditions. The air change per hour (ACH) was estimated to be around 25. The measured ambient (outdoor) temperature and relative humidity of each air filtration system combination test are listed as follows:

- Control – 73$^{o}$F and 55%
- MERV 8 - 53$^{o}$F and 87%
- MERV 8 + NBI - 62$^{o}$F and 61%
- MERV 8 + DBD - 62$^{o}$F and 58%
- MERV 8 + UVC - 79$^{o}$F and 48%
- MERV 13 - 66$^{o}$F and 66%
- MERV 13 + NBI - 61$^{o}$F and 56%
- MERV 13 + DBD - 56$^{o}$F and 62%
- MERV 13 + UVC - 70$^{o}$F and 58%
- HEPA - 61$^{o}$F and 67%
- HEPA + NBI - 62$^{o}$F and 63%
- HEPA + DBD - 64$^{o}$F and 64%
- HEPA + UVC - 64$^{o}$F and 61%

### 3.2 Volatile Organic Compounds (VOCs)

Figure 2 presents sample trended VOC percentages of each air filtration system combination test from each control output measured by the BELIMO sensors of PF-RA (red), RA (yellow), MA (blue), and SA (green) using Figure 1 (c) timeline. RA, MA, and SA stand for return, mixed, and supply airs, respectively. The VOC percentage is defined as the ratio of actual total VOCs and maximum possible total VOCs' concentrations. Outdoor temperature and relative humidity are also listed for each air filtration system combination test.

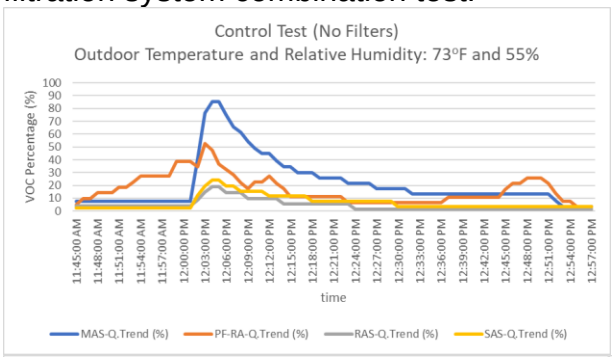


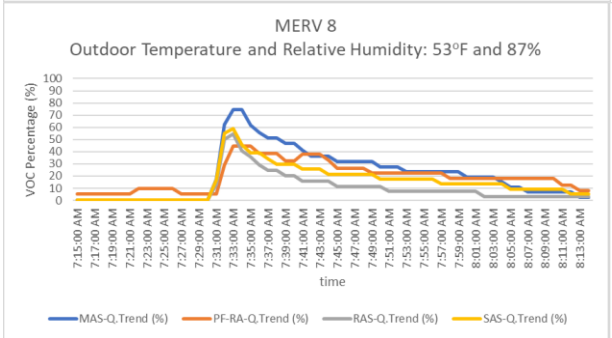


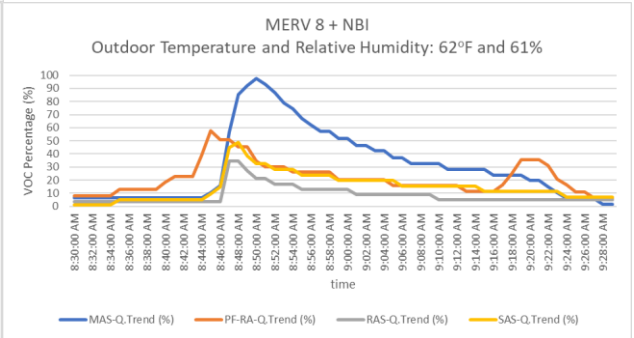


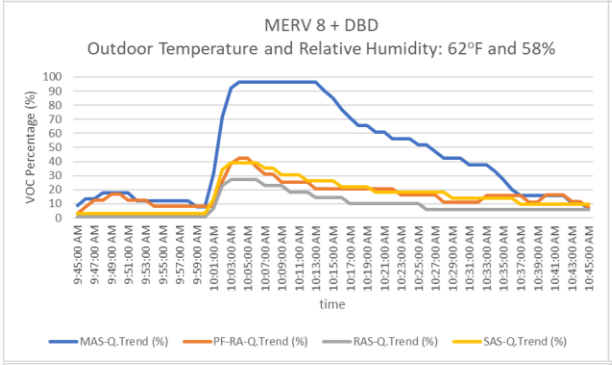


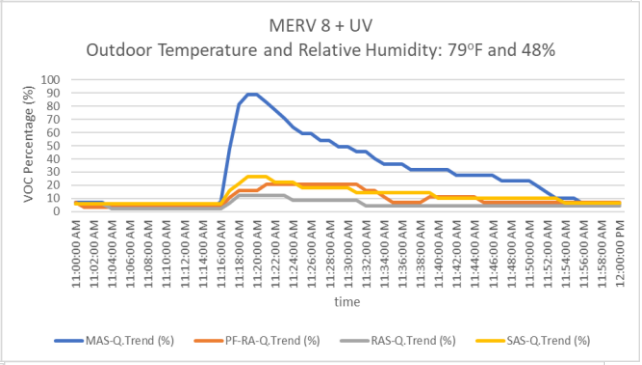


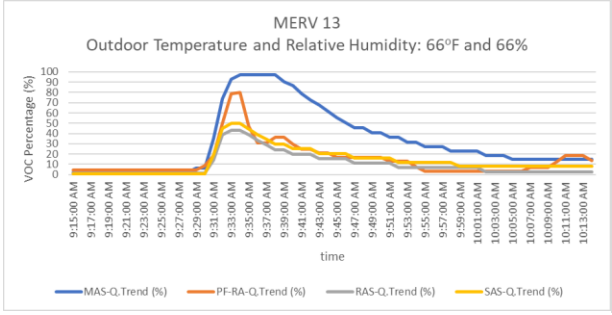


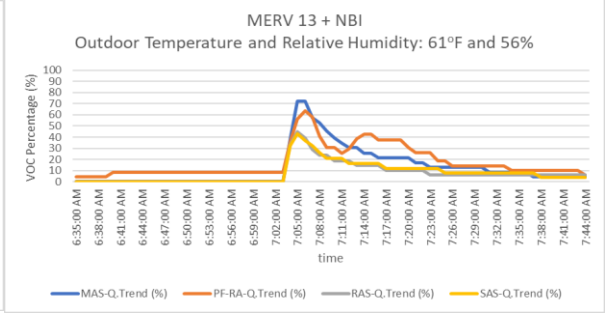

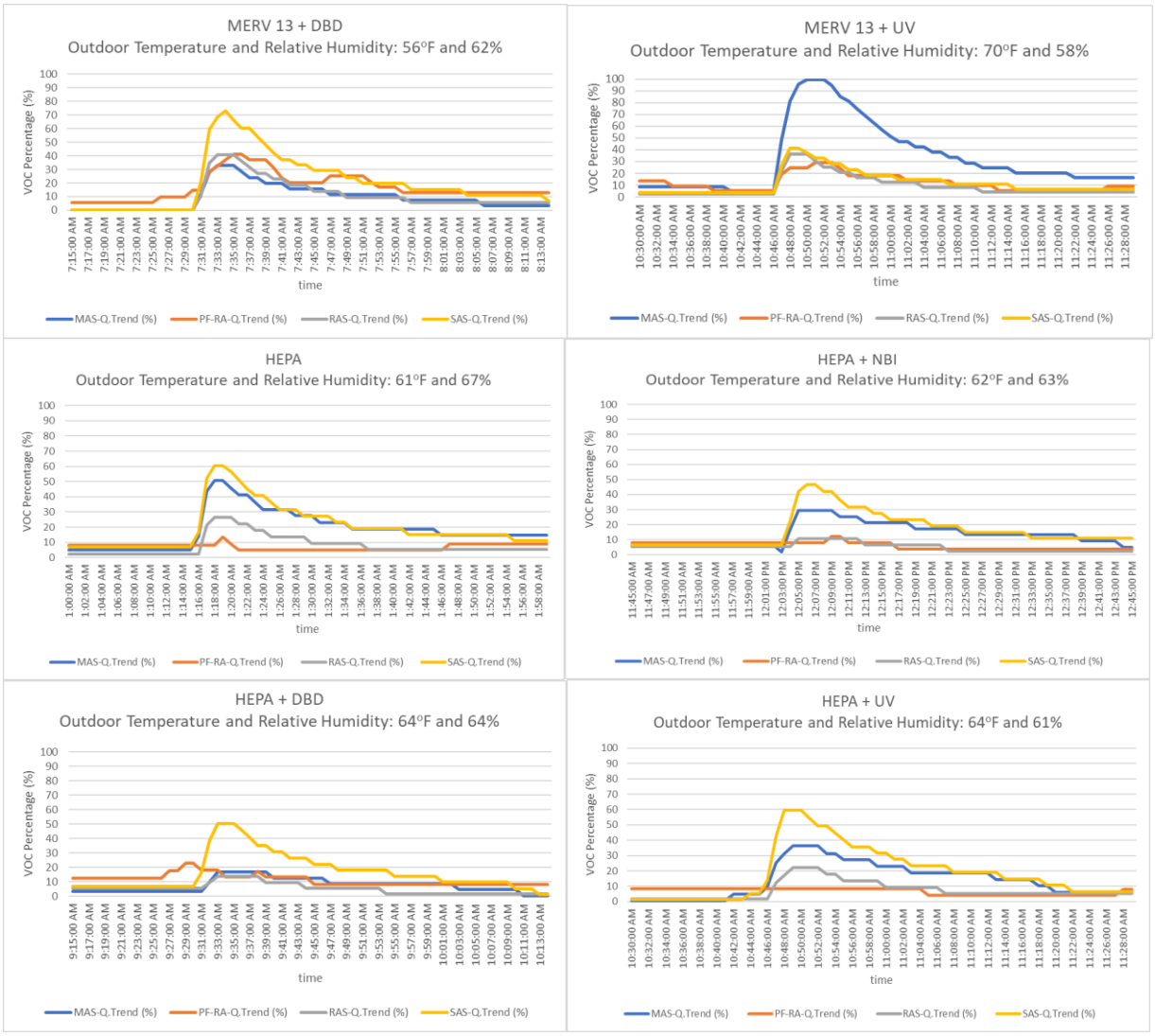


**Figure 2**. Trended VOC percentages of each air filtration system combination from BELIMO sensor outputs, 1-minute resolved data.

In the present phase of work, there was no mixed air but 100% return air because outside air opening was sealed closed. The location of each BELIMO IAQ sensor can be identified from Figure 1 (a). Generally, all sensors presented an increase followed by a decrease in the VOC percentage during the approximate one-hour test duration. The rising trend of the VOC percentage indicated a smoke introduction from a smoke hose output to the indoor space whereas the decreasing trend showed a smoke dissipation in both control (no filters, no BPI, and no UVC) and filtration system combination tests. These rising and falling trends of the VOC concentrations due to a contaminant source were consistent with the reported work of Demanega et al. [3]. In addition, Zeng et al. [2] reported that the downstream of an air-handler unit tended to carry higher VOC concentrations than its upstream and that findings were consistent with the present work results. In general, SA, MA, and RA VOC percentages decayed from their peak values until the fan was turned off. Interestingly and similarly, Kim et. al [4] performed an experiment using an air purifier only with manganese catalyst-coated filter for the decomposition of VOCs in an actual smoking room. The treatment

(removal) efficiency of cigarette-generated VOCs was found to be over 80% after thirty minutes of air purification [4]. Kim et. al. [4] also observed “natural decay” phenomena in which a natural reduction was exhibited in circulating only air without running an air-cleaning system. Those observations were consistent with the present decay of VOCs for a control or a physical filter only test condition. The VOC decay was realized when the gases were absorbed to the walls of the smoking house chamber and disappeared. To isolate the source of a variance to make a fair comparison between test systems, a normalization method is employed. To quantify the normalized VOC percentage reduction of each test case scenario, the VOC percentage reduction between its maximum percentage due to the smoke source and minimum percentage when the fan was shut off over the SA air duct location normalized by its recorded maximum VOC percentage were calculated.

Table 1 and Figure 3 show the normalized VOC percentage reduction test results of each filtration system combination measured at supply air duct location with the BELIMO sensor over the test duration. The last row of data represents the average of those listed normalized VOC percentage reduction test results for each air treatment technology. Table 1 shows that a lesser filter such as the MERV 13 filter combined with the NBI technology outperformed HEPA filter combined with the NBI technology. The MERV 13 filter combined with either BPI technology outperformed the HEPA filter by itself. Overall, MERV 13 filter combined with the NBI manufacturer A technology had the best performance on VOC concentration reduction among all test combinations. Results reported that NBI device delivered the best performance on reducing VOC concentration (at least a surplus of 3 in terms of normalized VOC percentage reduction compared with other air treatment technologies and close to a surplus of 5 in terms of normalized VOC percentage reduction compared with that of without air treatment technology), followed by DBD device, filter without having an air treatment technology, and the least performance went to UVC lamp.

**Table 1**. Normalized VOC percentage reduction test results of each system combination at supply air duct location.

| | Without Air Treatment Technology | **NBI** | **DBD** | UVC |
|---|---|---|---|---|
| MERV 8 | 0.70 | 0.76 | 0.65 | 0.62 |
| **MERV 13** | 0.76 | 0.82 | 0.79 | 0.74 |
| **HEPA** | 0.75 | 0.76 | 0.80 | 0.75 |
| Average | 0.73 | 0.78 | 0.75 | 0.70 |

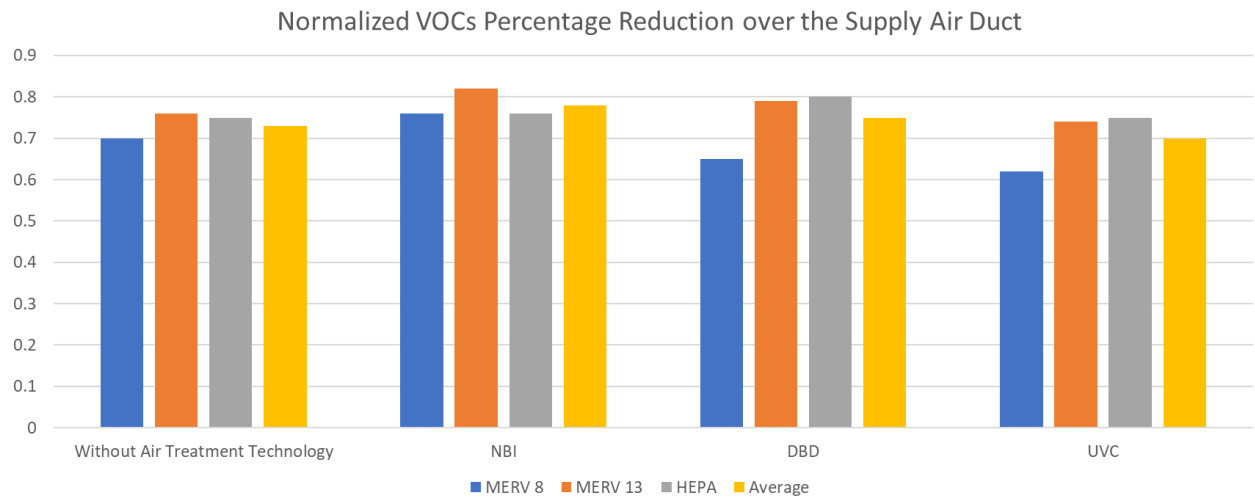


**Figure 3.** Normalized VOCs percentage reduction of air filters combined with or without air treatment technologies over the supply air duct

Figure 4 reports sample trended formaldehyde (part of VOC) concentration data of each air filtration system combination measured from TEMTOP indoor air quality handheld monitors with 1-minute resolved data. The trended formaldehyde concentration data of both supply and return air locations were generally similar to the trends of air VOC percentage data, which the VOC concentration rose to a peak value before it decreased. The rising and falling trends of formaldehyde concentration data due to the smoke source were consistent with the findings of Demanega et al. [3]. To determine the effectiveness of an air treatment technology, the formaldehyde concentration reduction between the recorded maximum and minimum values after the smoke was injected normalized by its maximum concentration value was quantified. Figure 5 shows that the best air treatment technology is the NBI device (0.32 normalized reduction), followed by DBD device (0.25 normalized reduction), UVC light (0.2387 normalized reduction), and no air treatment technology (0.2386 mg/m$^3$ normalized reduction).

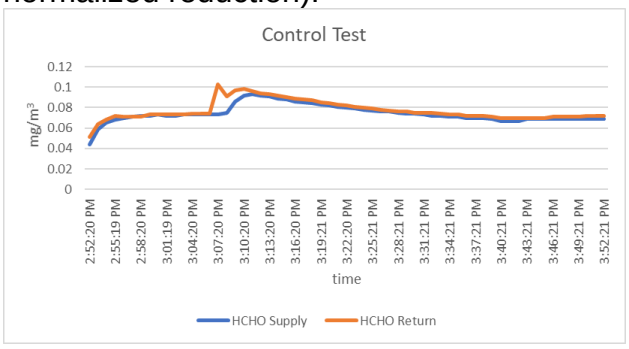

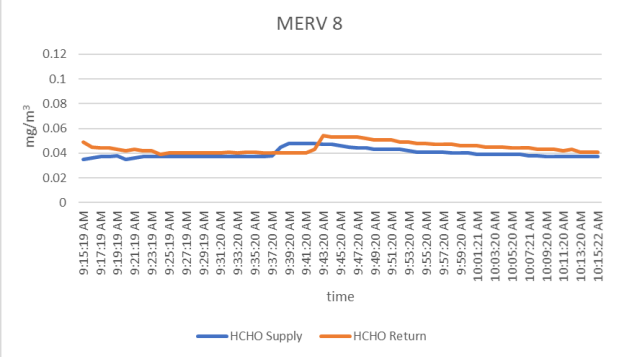
MERV 8
mg/m³
time
HCHO Supply
HCHO Return

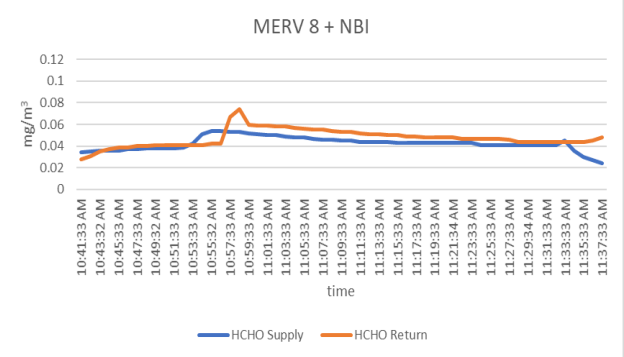
MERV 8 + NBI
mg/m³
time
HCHO Supply
HCHO Return

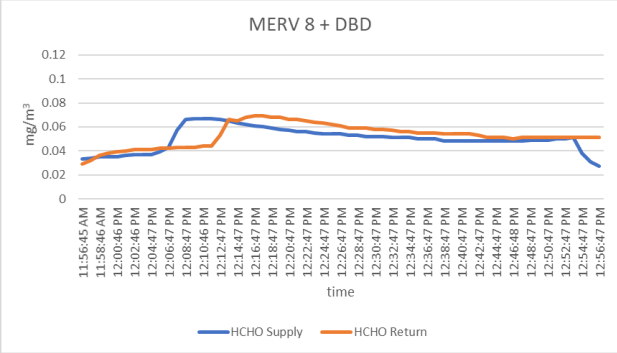
MERV 8 + DBD
mg/m³
time
HCHO Supply
HCHO Return

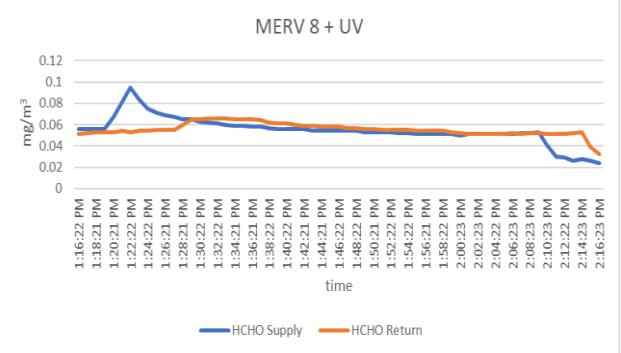
MERV 8 + UV
mg/m³
time
HCHO Supply
HCHO Return

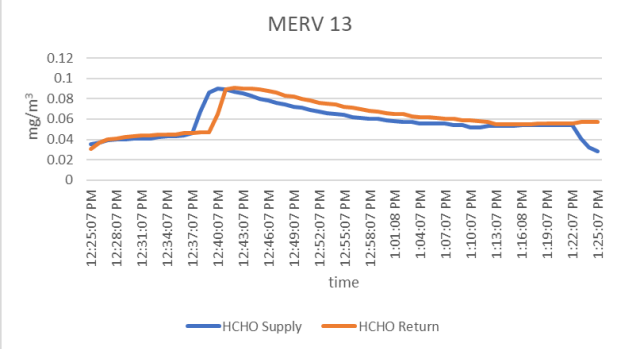
MERV 13
mg/m³
time
HCHO Supply
HCHO Return

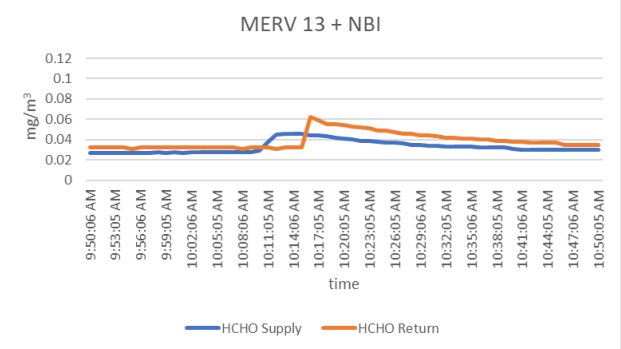
MERV 13 + NBI
mg/m³
time
HCHO Supply
HCHO Return

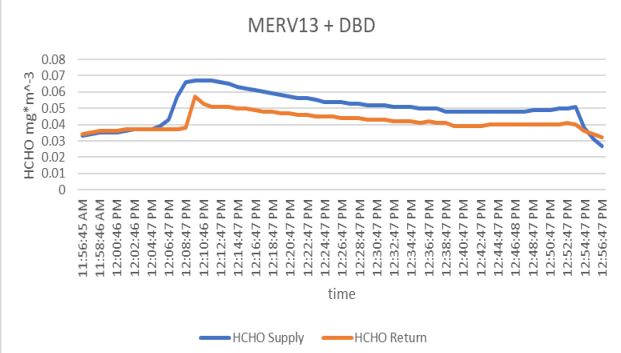
MERV13 + DBD
HCHO mg*m^-3
time
HCHO Supply
HCHO Return

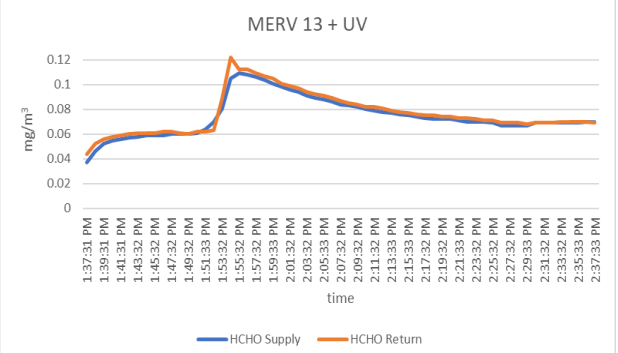
MERV 13 + UV
mg/m³
time
HCHO Supply
HCHO Return

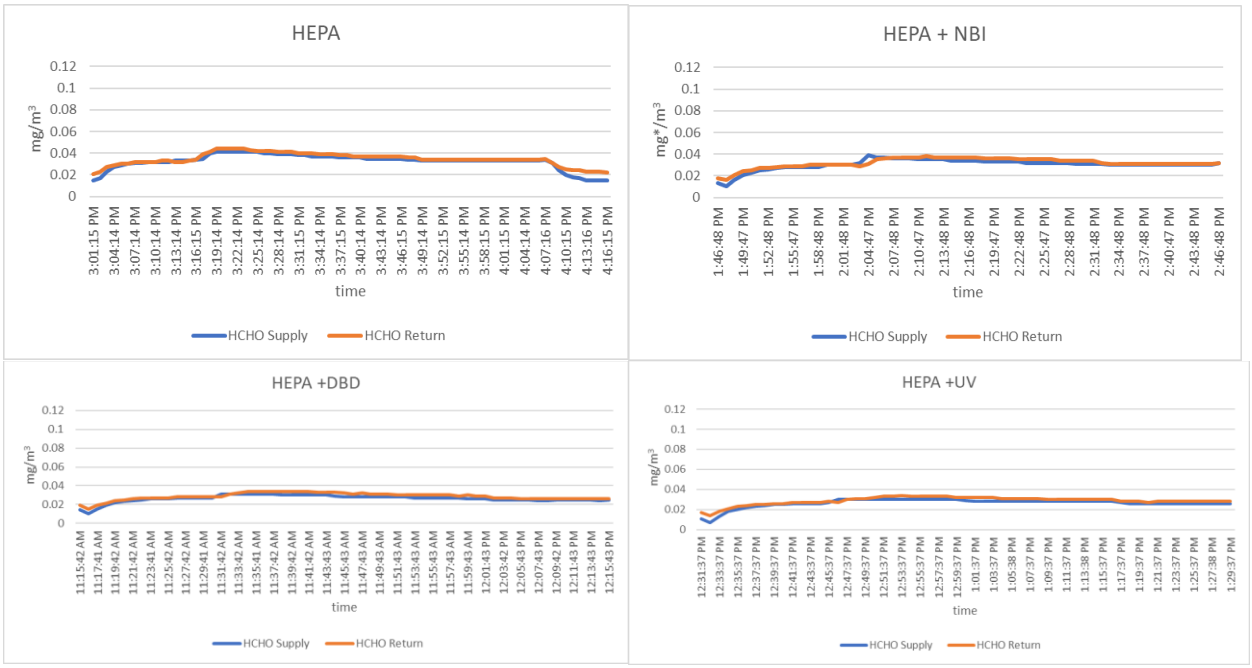


**Figure 4**. Trended formaldehyde (part of VOC) concentration data of each air filtration system combination without cooling coil from TEMTOP IAQ handheld monitors, 1-minute resolved data.

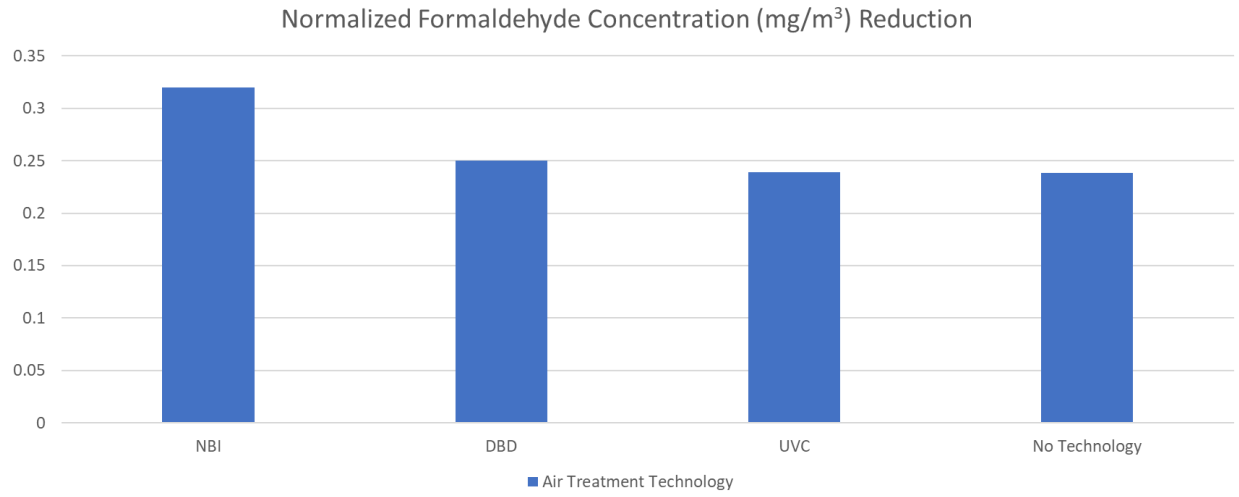


**Figure 5.** Normalized formaldehyde concentration reduction of different air treatment technology

### 3.3 Carbon Dioxide

Figure 6 presents sample trended $CO_2$ (ppm) data of each air filtration system combination from control outputs and the $CO_2$ (ppm) data. It is noted that the VOC percentage was not measured by the BELIMO indoor zone sensor. Figure 6 generally shows that the $CO_2$ (ppm) data were monotonous but with slight reductions from each control output with Zone (light blue) reading at the highest concentration followed by RA (yellow) and MA (orange). $CO_2$ (ppm) data of SA (gray) and PF-RA (blue) were generally the lowest depending on whether air treatment technology was used. Interestingly, the air treatment technology was observed to consistently yield the

smallest $CO_2$ concentration at the SA station especially when MERV 13 and HEPA filters were used otherwise the $CO_2$ concentration at the SA station generally exceeded the $CO_2$ concentration at the PF-RA station. The $CO_2$ (ppm) data generally ranges between 460 and 700 ppm. This monotonous and slight reducing $CO_2$ concentration profile was also observed in the work of Pistochini et al. [5] when there were no occupants in an indoor environment.

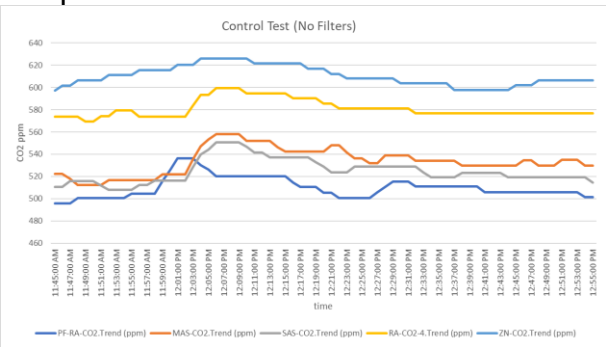


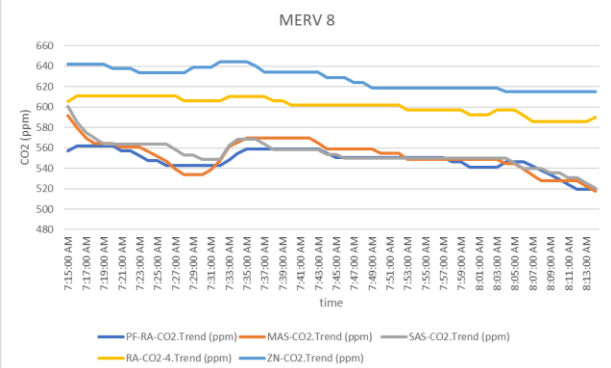


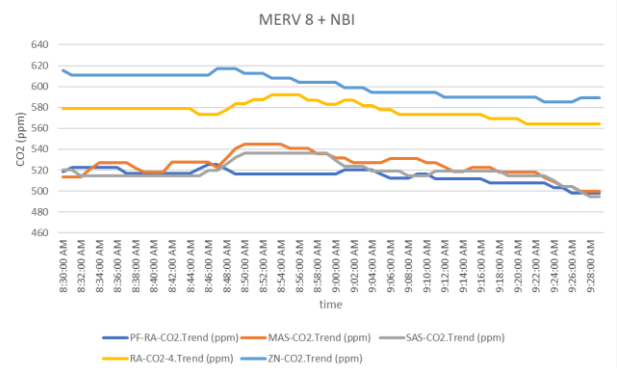


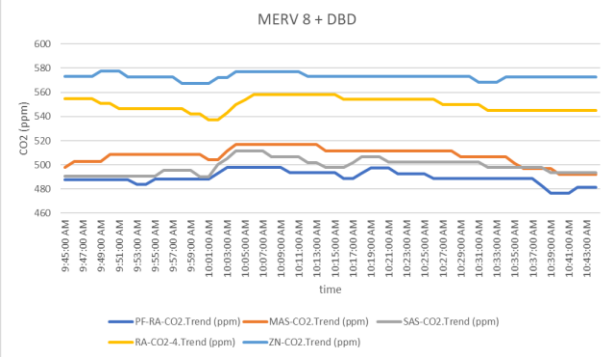


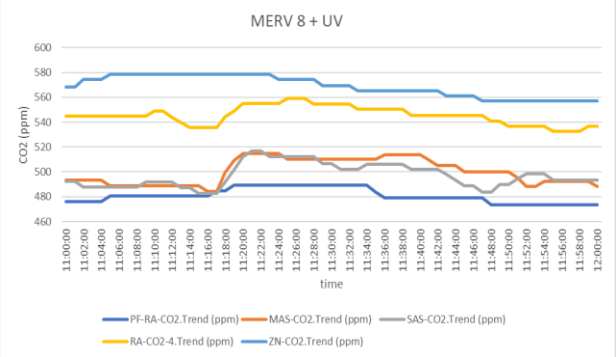


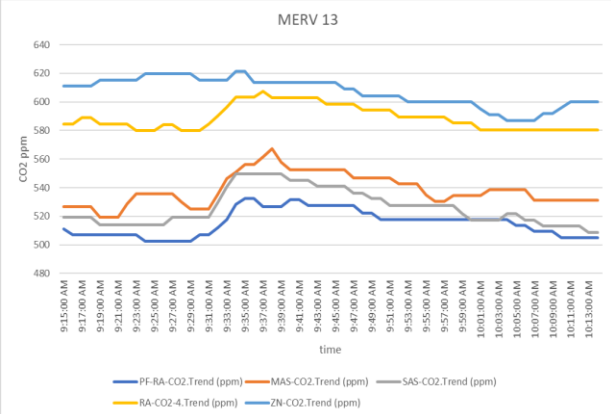


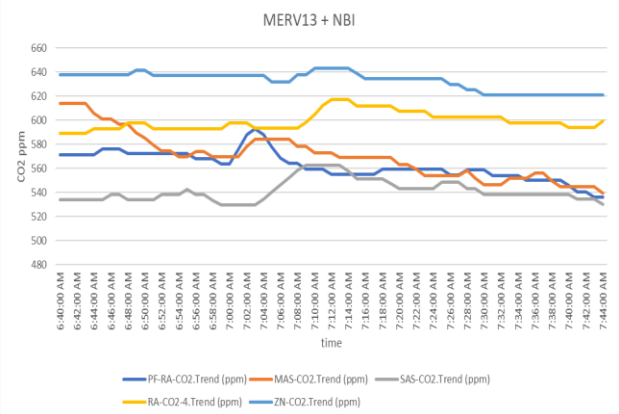

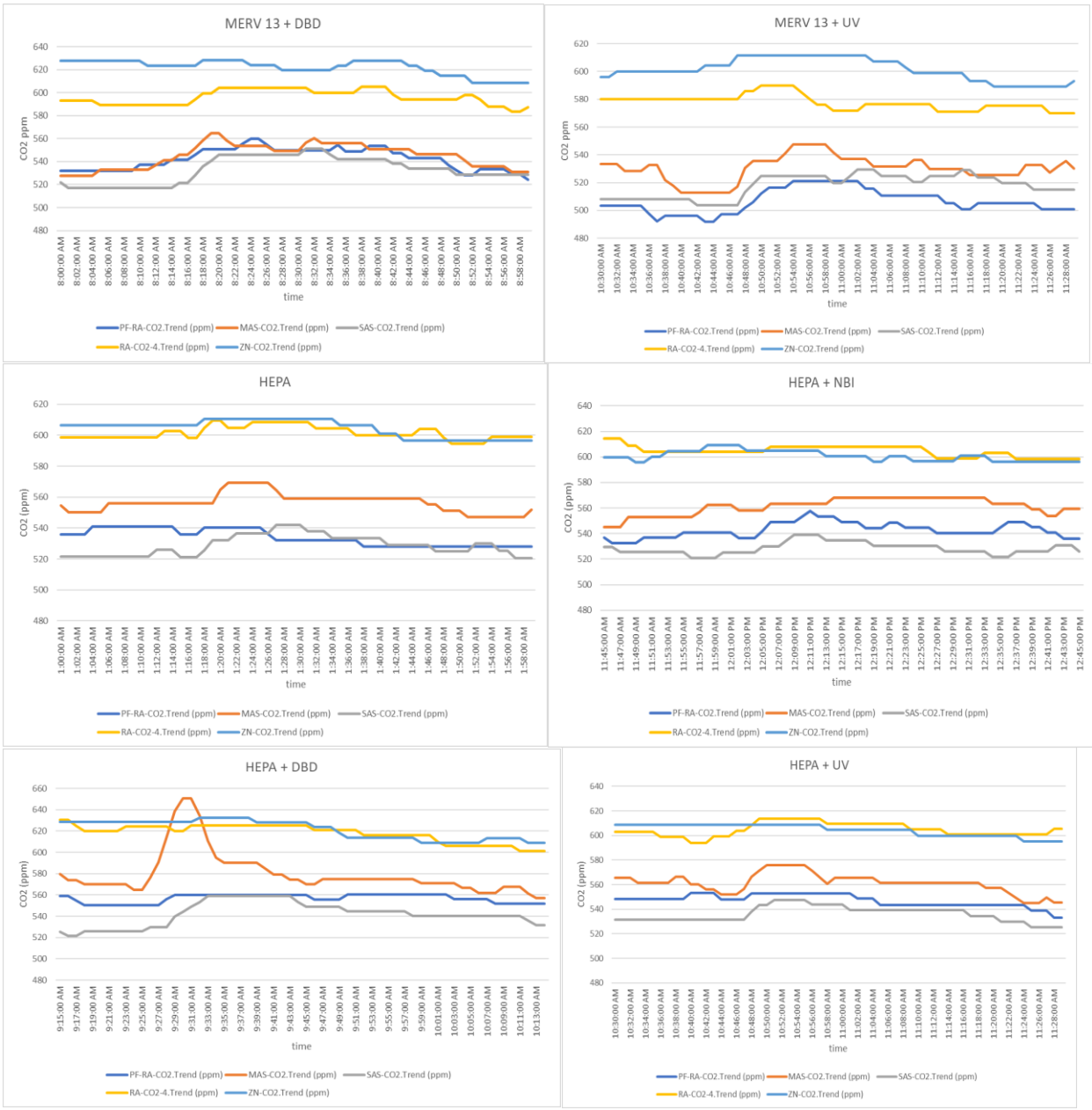


**Figure 6**. Trended $CO_2$ (ppm) data of each air filtration system combination from BELIMO sensor outputs, 1-minute resolved data.

### 3.4 Particulate Matters

Figure 7 shows sample trended PM 2.5 data of each air filtration system combination from TEMTOP indoor air quality handheld monitors with 1-minute resolved data. Both supply and return air PM 2.5 profiles were recorded and plotted for each test scenario. Both profiles demonstrated a rising and decaying particulate matter concentrations due to the five-minute smoke introduction. The reductions of PM 2.5 concentrations with ionizer on were also observed in the work of Pushpawela et al. [6]. Generally, both supply and return air PM 2.5 have similar maximum and minimum recorded values from each test. The supply air PM 2.5 data were used for analysis as discussed in the following.

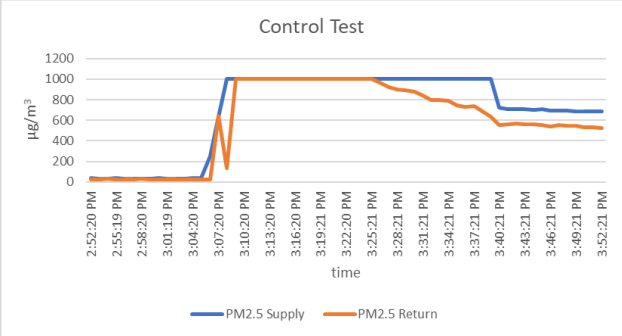
Control Test
µg/m³
time
PM2.5 Supply
PM2.5 Return

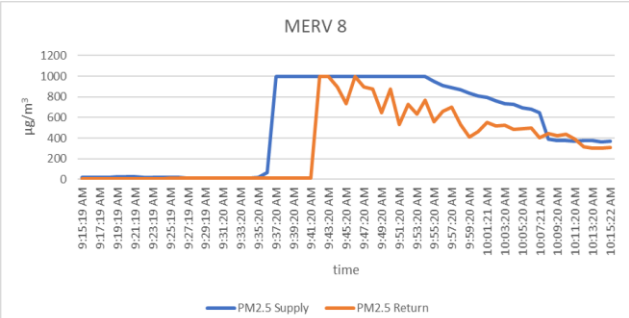
MERV 8
µg/m³
time
PM2.5 Supply
PM2.5 Return

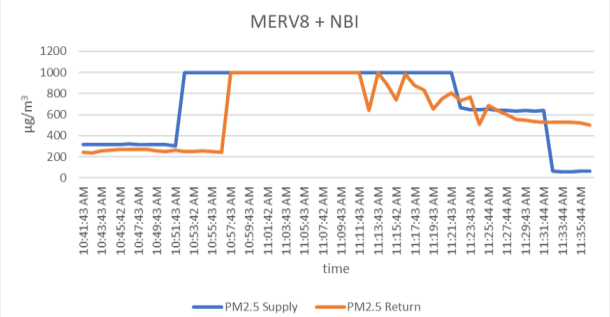
MERV8 + NBI
µg/m³
time
PM2.5 Supply
PM2.5 Return

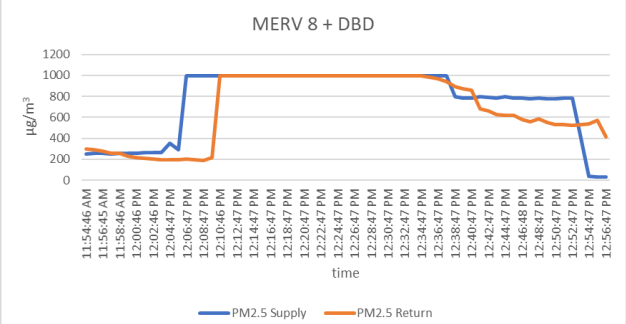
MERV 8 + DBD
µg/m³
time
PM2.5 Supply
PM2.5 Return

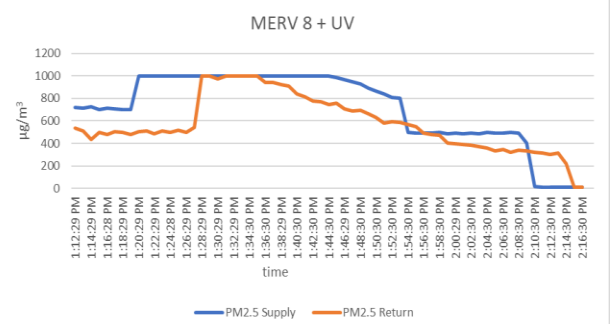
MERV 8 + UV
µg/m³
time
PM2.5 Supply
PM2.5 Return

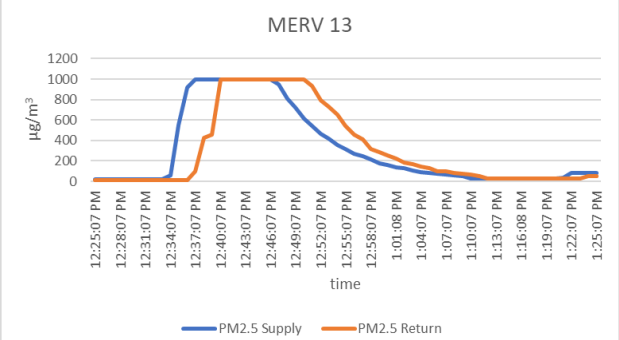
MERV 13
µg/m³
time
PM2.5 Supply
PM2.5 Return

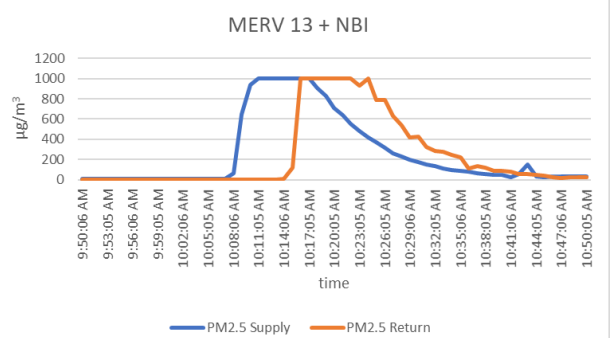
MERV 13 + NBI
µg/m³
time
PM2.5 Supply
PM2.5 Return

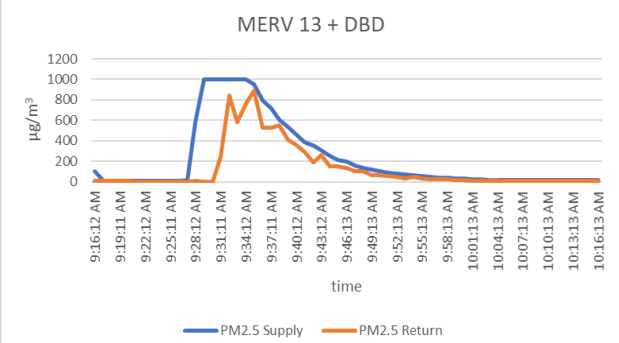
MERV 13 + DBD
µg/m³
time
PM2.5 Supply
PM2.5 Return

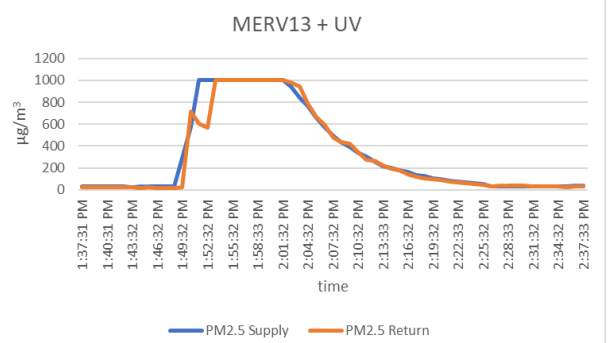
MERV13 + UV
µg/m³
time
PM2.5 Supply
PM2.5 Return

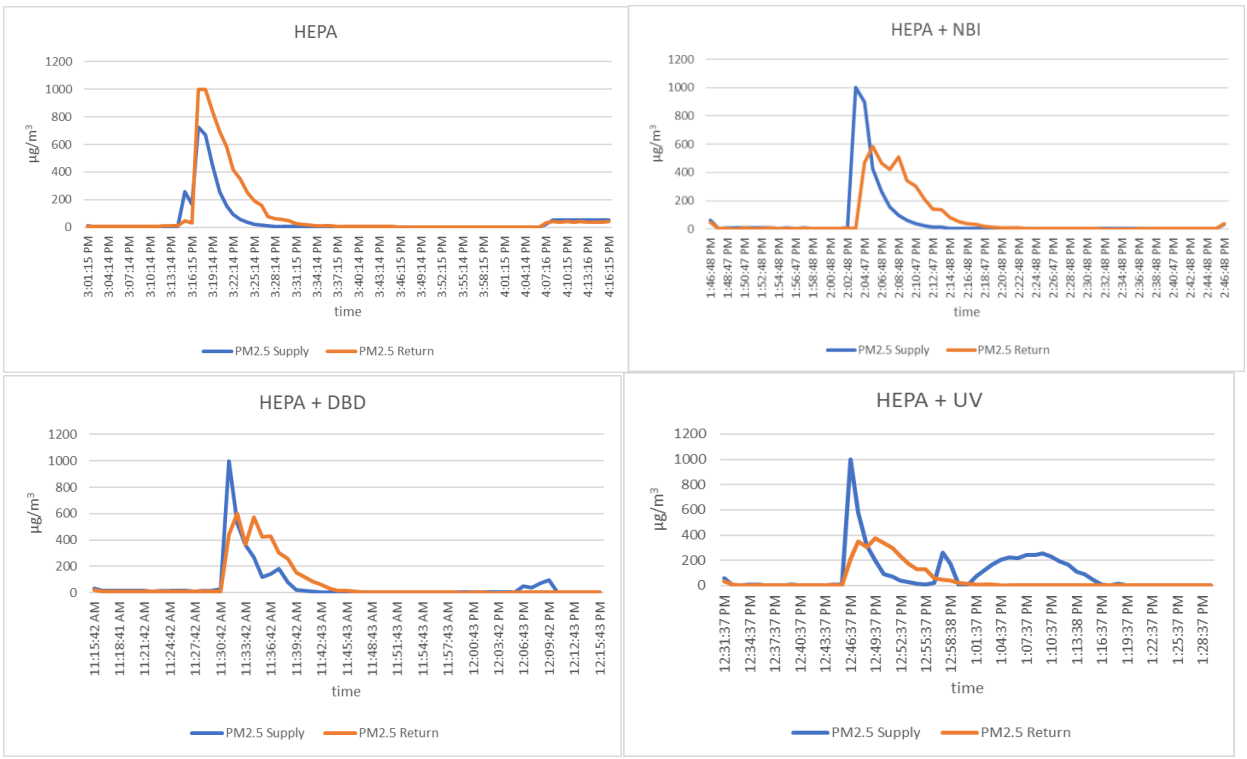


**Figure 7**. Trended PM 2.5 data of each air filtration system combination from TEMTOP IAQ handheld monitors, 1-minute resolved data.

Table 2 presented the maximum and minimum PM 2.5 test results before and when fan was shut off, respectively, and removal efficiency of each system combination measured at the supply air duct based on the measured maximum and minimum PM 2.5 values. Figure 8 presents the removal efficiency of each air treatment technology combined with an air filter. Interestingly, MERV 13 lesser physical filter combined with the DBD device closely matches the performance of a HEPA filter with and without the BPI device in filtering the fine particulate matters. MERV 8 systems show the worst performance among all whereas HEPA systems consistently show the best performance compared with others in removing fine particulate matters.

**Table 2**. Maximum and minimum PM 2.5 test results before and when fan was shut off, respectively, and removal efficiency of each system combination measured at the supply air duct based on the measured maximum and minimum PM 2.5 values.

| | Maximum Before Fan Was Shut Off ($\mu g/m^3$) | Minimum When Fan Was Shut Off ($\mu g/m^3$) | Removal Efficiency (%) |
|---|---|---|---|
| MERV8 | 999 | 647 | 35 |
| MERV8+NBI | 999 | 506 | 49 |
| MERV8+DBD | 999 | 780 | 22 |
| MERV8+UV | 999 | 488 | 51 |
| | | | |
| MERV13 | 999 | 64 | 93 |

| | | | |
|---|---|---|---|
| MERV13+NBI | 999 | 70 | 93 |
| MERV13+DBD | 999 | 11 | 98.8 |
| MERV13+UV | 999 | 70 | 93 |
| | | | |
| HEPA | 671 | 3 | 99.5 |
| HEPA+NBI | 999 | 3 | 99.7 |
| HEPA+DBD | 999 | 3 | 99.7 |
| HEPA+UV | 999 | 48 | 95 |

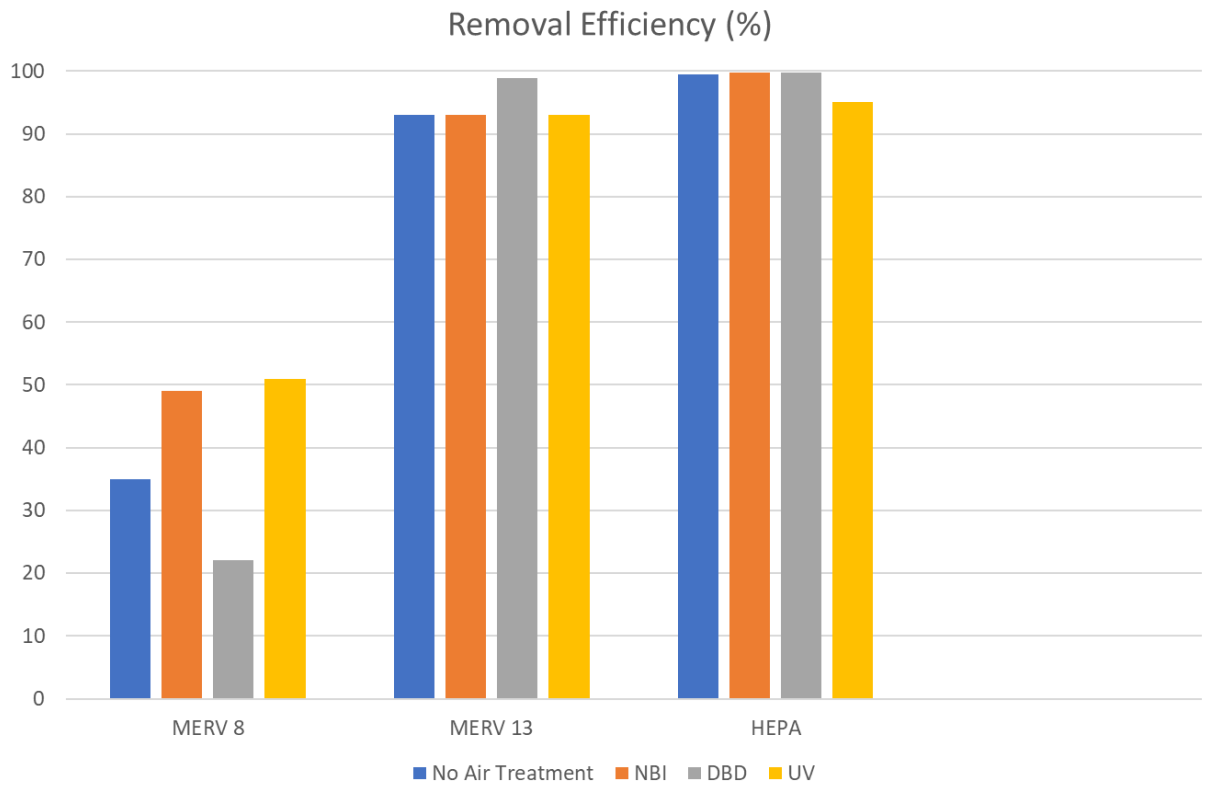


**Figure 8.** Removal efficiency of each air treatment technology combined with an air filter

## 4. Conclusions and Future Work

The effect of air treatment technology with a physical air filter on the IAQ of a 400 $ft^2$ house with a woodchip-based smoke source was assessed in a fully recirculated indoor airflow environment with outside air opening sealed closed in the present work. Air treatment technologies include BPI devices and UVC light whereas physical air filters include MERV and HEPA filters were studied. Mitigation of VOC, $CO_2$, and PM 2.5 concentrations from various sensor/monitor outputs was evaluated. To conclude, results showed that the BPI air treatment device combined with a physical filter generally delivered a better performance in reducing VOC and $CO_2$ concentrations at the supply air duct compared with those filters without any BPI device. In addition, MERV 13 lesser physical air filter combined with the DBD device closely matched the performance of a HEPA high efficiency filter with and without the BPI device in filtering

the fine particulate matters. UVC light did not appear to be effective in mitigating VOC and $CO_2$ concentrations.

Since the phase one of this IAQ research project showed promising results that a DBD device was able to enhance the effectiveness of the MERV filters such that smoke contaminants are reduced to a level that meets the HEPA testing criteria without outside air, the second phase of work will be decided by the ASHRAE San Joaquin research committee, and it will be most likely performing tests with contaminant sources of steam and/or carbon dioxide gases. The test will consist of testing the top two system combinations discovered from this phase one of project as follows:

- MERV 13 + DBD
- MERV 13 + NBI

In addition, the test will include testing another two systems such as the control and HEPA. Each test will run for a minimum period of 30 minutes. The room will be configured in such a way that only one fan will be used, cooling coil will not be used, and the contaminants introduced into the system will be done inside the room. The effect of using the combined technologies on mitigating and filtering the VOC, $CO_2$, and PM 2.5 concentrations given a contaminant source in the indoor environment will be studied.

## Acknowledgment

The authors would like to acknowledge the research funding support and air handler equipment donation given by the ASHRAE San Joaquin Chapter for this IAQ research project. The authors thank the President of Net Positive Consulting Engineers Mr. Jonathan Schlundt for serving as the point of contact for the ASHRAE San Joaquin and the Johnson Controls Company for BELIMO sensor installation.

## References

1. Fresno State indoor air quality research contract agreement, 2021.
2. Zeng, Y., Manwatkar, P., Laguerre, A., Beke, M., and Kang, I., 2021, “Evaluating a commercially available in-duct bipolar ionization device for pollutant removal and potential byproduct formation”, Building and Environment, 195, 107750.
3. Demanega, I., Mujan, I., Singer, B.C., Andelkovic, A.S., Babich, F., and Licina, D., 2021, “Performance assessment of low-cost environmental monitors and single sensors under variable indoor air quality and thermal conditions”, Building and Environment, 187, 107415. https://doi.org/10.1016/j.buildenv.2020.107415
4. Kim, M., Jung, H., Park, E., Jurng, J., 2020, “Performance of an air purifier using a MnOx/TiO2 catalyst-coated filter for the decomposition of aldehydes, VOCs and ozone: An experimental study in an actual smoking room”, Building and Environment, 186, 107247. https://doi.org/10.1016/j.buildenv.2020.107247
5. Pistochini, T., Mande, C., Modera, M., Outcalt, S., Sanguinetti, A., Chan, R. W., Dutton, S., Singer, B., and Li, X., 2020, “Improving ventilation and indoor environmental quality in California schools”, Energy Research and Development (500), CEC-500-2020-049.
6. Pushpawela, B., Jayaratne, R., Nguy, A., Morawska, L., 2017, “Efficiency of ionizers in removing airborne particles in indoor environments”, Journal of Electrostatics, 90, pp. 79-84. http://dx.doi.org/10.1016/j.elstat.2017.10.002

**Appendix of Indoor Air Quality Technical Report**

(a) Air handler equipment (b) IAQ sensors (orange boxes)

**Figure 9**. Air handler equipment and IAQ sensors

(a) Return air quality monitor (b) Supply air quality monitor

**Figure 10**. Return and supply air quality monitors

(a) Smoke house and outlet (green)  (b) Smoke injection

**Figure 11**. Smoke house, outlet, and injection in the house chamber


**Figure 12**. Bipolar ionization devices installed at the supply air duct

VERIFIED
ZERO OZONE

Intertek does hereby certify that an independent assessment has been conducted on behalf of

# ATMOSAIR

**Certificate Number: 104722638GRR-001a**
Certification Issued: 17 June 2021

Initial Verification Date: 18 September 2020
Certificate Valid Until: 16 September 2022

**Applicant Address:** **418 Meadow Street, Suite 204**
**Fairfield, CT 06824 USA**

**Product Category:** **Appliances & Electronics**

**Product Details:** **See Appendix**

**Conformance Criteria:** **Conforms to UL 2998 (3rd Edition, July 10, 2020) clause 6.2, emittance of ozone not exceeding a concentration of 0.005 ppm.**

**Issuing Office Name & Address:** **Intertek Testing Services NA, Inc.**
**4700 Broadmoor Ave SE, Suite 200**
**Kentwood, MI 49512 USA**
**Ph: +1-616-656-7401**

Jesse Ondersma
Certification Officer
17 June 2021


**Figure 13.** UL2998 certificate 2021 of the DBD device